Diogo Alexandre Castro Vaz

Licenciatura em Ciências de Engenharia
de Micro e Nanotecnologias

Magnetotransport properties of metal/$LaAlO_3$/$SrTiO_3$ heterostructures

Dissertação para obtenção do Grau de Mestre em
Engenharia de Micro e Nanotecnologias

Orientador: Dr. Manuel Bibes, Senior Scientist, Unité Mixté de Physique CNRS/Thales, Paris, France

Co-orientador: Dr. Rodrigo Martins, Professor Doutor, Faculdade de Ciências e Tecnologia da Universidade Nova de Lisboa, Portugal

Júri:

Presidente: Doutor Hugo Manuel Brito Águas, Professor Auxiliar do Departamento de Ciência dos Materiais da Faculdade de Ciências e Tecnologia da Universidade Nova de Lisboa

Vogais: Doutor José Paulo Moreira dos Santos, Professor Associado com Agregação do Departamento de Ciência de Física da Faculdade de Ciências e Tecnologia da Universidade Nova de Lisboa

Doutor Rodrigo Ferrão de Paiva Martins, Professor Catedrático do Departamento de Ciência dos Materiais da Faculdade de Ciências e Tecnologia da Universidade Nova de Lisboa

FACULDADE DE CIÊNCIAS E TECNOLOGIA
UNIVERSIDADE NOVA DE LISBOA

Setembro 2015

Magnetotransport properties of metal/$LaAlO_3$/$SrTiO_3$ heterostructures.

"I am not discouraged, because every wrong attempt discarded is another step forward."

Thomas Edison

Acknowledgements

I would firstly like to thank Manuel Bibes for the guidance, help and friendship throughout this project. Although this was a completely new subject to me, he made sure that I always felt at home. To Agnès Barthélémy for being my unofficial supervisor and for her experience and fruitful discussions. To Edouard Lesne for all the help and encouragement. Without him and his PdD work I would have probably spent the full six months just trying to grow one good $LaAlO_3/SrTiO_3$ sample. To all the friends from the oxide group for putting up with my basic questions, cheering me up in the worst possible days and teaching me how to deal with French bureaucracies.

Um especial agradecimento ao professor Rodrigo Martins. Sem a sua ajuda e orientação não teria sido possível sequer começar este projecto. Um obrigado também a todo o corpo docente que me acompanhou durante os últimos cinco anos. Todos os relatórios, discussões e difíceis aulas às 8 da manhã revelaram-se bastante úteis.

Um enorme obrigado a todas os colegas do mestrado integrado. Creio que não teria sido possível acabar o curso e manter um estado mental saudável sem a vossa presença.

To all the amazing friends and neighbors from Maison de Norvège. For the cultural exchange, for the amount of weird stuff that happened in the house, for the pleasure of having a beer/glass of wine in the end of a long day of work, for the dramas with the Cité night security, for the "deer incident" and for those unforgettable long dinners in the balcony. These six months passed by so fast because of you guys.

À minha segunda família do grande reino do Basolho (e associados). Acho que o universo nunca antes juntou na mesma casa pessoas tão incríveis. Pelas longas conversas, por pensarmos todos de forma assustadoramente igual, pelas festas, pelos sucessos/derrotas emocionais e por todas as memórias que ficaram dos melhores cinco anos de sempre. Podemos estar longe agora mas isto ainda não acabou!

Finalmente, e porque o melhor fica para o fim, queria agradecer à minha família, porque não poder estar com eles durante seis meses custou mas o resultado valeu a pena. Um gigante obrigado às tias, tios, primos, primas e em especial aos meus pais, por me tornarem na pessoa que sou hoje e por me deixarem sempre seguir as minhas ambições e me fazerem acreditar que tudo é possível.

Abstract

The quasi two-dimensional electron gas (q2DEG) hosted in the interface of an epitaxially grown lanthanum aluminate ($LaAlO_3$) thin film with a TiO_2-terminated strontium titanate ($SrTiO_3$) substrate (001) has been massively studied in the last few years. The confinement of mobile electrons to within a few nanometers from the interface, superconductive behavior at low temperatures and electron mobility exceeding 1000 $cm^2/(V.s)$ make this system an interesting candidate to explore the physics of spin injection and transport. However, due to the critical thickness for conduction of 4 unit cells (uc) of $LaAlO_3$, a high tunneling resistance hampers electrical access to the q2DEG, preventing proper injection of spin polarized current.

Recently, our group found that depositing a thin overlayer of Co on $LaAlO_3$ reduces the critical thickness, enabling conduction with only 1 uc of $LaAlO_3$. Two scenarios arise to explain this phenomenon: a pinning of the Fermi level in the metal, inducing charge transfer in the $SrTiO_3$; the creation of oxygen vacancies at the interface between $LaAlO_3$ and the metal, leading to an n-type doping of the $SrTiO_3$.

In this dissertation, we will report on magnetotransport of metal/$LaAlO_3$/$SrTiO_3$ (metal: Ti, Ta, Co, Py, Au, Pt, Pd) heterostructures with 2 uc of $LaAlO_3$ studied at low temperatures (2 K) and high magnetic fields (9 T). We have analyzed the transport properties of the gas, namely, the carrier concentration, mobility and magnetotransport regime and we will discuss the results in the light of the two scenarios mentioned above.

Keywords: Interfaces, perovskite, oxides, metals, critical thickness, LaAlO3, SrTiO3, magnetotransport.

Resumo

O gás de electrões quase bidimensional (q2DEG) alojado na interface de um filme fino de aluminato de lântanio ($LaAlO_3$) epitaxialmente crescido num substrato de titanato de estrôncio ($SrTiO_3$) com terminação TiO_2 (001) tem sido intensamente estudado nos últimos anos. O confinamento de electrões móveis a poucos nanometros da interface, superconductividade a baixas temperaturas e mobilidades (de electrões) superiores a 1000 $cm^2/(V.s)$ tornam este sistema um candidato interessante para exploração da física de injecção e transporte de spin. No entanto, devido à espessura crítica para condução de 4 células unitárias (uc) de $LaAlO_3$, uma alta resistência elétrica de tunelamento impede o acesso ao q2DEG, impossibilitando injecção adequada de correntes de spin polarizado.

Recentemente, o nosso grupo descobriu que a deposição de uma fina camada exterior de cobalto (Co) reduz a espessura crítica, permitindo condução com apenas 1 uc de $LaAlO_3$. Dois cenários surgem para explicar este fenómeno: um *pinning* do nível de Fermi no metal que induz transferência de cargas para o $SrTiO_3$; a criação de vazios de oxigénio na interface entre $LaAlO_3$ e o metal que conduz a uma dopagem tipo n do $SrTiO_3$.

Nesta tese, vamos apresentar resultados de magnetotransporte em heteroestruturas metal/$LaAlO_3$/$SrTiO_3$ (metal: Ti, Ta, Co, Py, Au, Pt e Pd) com 2 uc de $LaAlO_3$, estudadas a baixas temperatures (2K) e altos campos magnéticos (9T). A análise das propriedades do q2DEG formado terá em conta a concentração de portadores, mobilidade e regime de magnetotransporte e a sua formação será discutida em função dos dois cenários mencionados acima.

Palavras-chave: Interfaces, perovskite, óxidos, metais, espessura crítica, LaAlO3, SrTiO3, magnetotransporte

Contents

Table of Figures

Table of Acronyms

q2DEG	Quasi Two-Dimensional Electron Gas
CB	Conduction Band
VB	Valence Band
TMP	Turbo Molecular Pump
RP	Rotary Pump
IR	Infrared
CCD	Charge-Coupled Device
AFM	Atomic Force Microscopy
CT-AFM	Conductive Tip Atomic Force Microscopy
PLD	Pulsed Laser Deposition
RHEED	Reflection High-Energy Electron Diffraction
WL	Weak Localization
WAL	Weak Antilocalization
SOI	Spin-Orbit Interaction
ASO	Atomic Spin-Orbit
MIGS	Metal-Induced Gap States
PWD	Potential Well Depth
MR	Magnetoresistance
MC	Magnetoconductance
XPS	X-Ray Photoelectron Spectroscopy

Table of Symbols

Q	Charge
V	Electrostatic Potential
E	Electric Field
uc	Unit Cell
t_c	Critical Thickness
f_o	Focal Length
R_q	Root Mean Square Surface Roughness
j	Current Density
R_{xx}	Longitudinal Resistance
R_S	Sheet Resistance
f	Van der Pauw Correction Factor
$\boldsymbol{F}$	Lorentz Force vector
q	Carrier Charge
$\boldsymbol{E}$	Electric Field vector
$\boldsymbol{v}$	Carrier Velocity vector
$\boldsymbol{B}$	Magnetic Field vector
ρ_{xy}	Transverse Resistivity
V_H	Hall Voltage
I	Current
R_{xy}	Transverse Resistance

$\underline{\underline{\boldsymbol{\rho}}}$	Tensor of Resistivity
$\boldsymbol{j}$	Current Density vector
R_H	Hall Coefficient
n_s	Sheet Carrier Concentration
σ_{xx}	Longitudinal Conductivity
d	Thickness
μ_H	Hall Mobility
σ_{2D}^{0}	Sheet Conductance at Zero Magnetic Field
χ	Electron Affinity
E_g	Bandgap
E_F	Fermi Energy
V_O	Vacuum Level
ϕ_{SB}	Schottky Barrier Height
ϕ	Work Function
ϕ_C	Critical Work Function
ΔH_0	Enthalpy of Formation

1

Introduction

Our lives have been completely overrun by technology. The fact that nowadays the average consumer spends more time using their phone or laptop than sleeping is encouraging the electronics industry to invest more and more each year into new developments. So far, silicon has been the backbone of the entire industry, but an inevitable mitigation of its usage has always been clear. Further component downsizing will compromise performance and new solutions must be found. Oxide electronics has shown remarkable properties and capabilities way beyond silicon. Specifically, interfaces between complex oxides exhibit new and unusual electronic phases that can be used to develop spintronic devices, where spin polarized electrons are used to carry information. This dissertation is devoted to the study of the high mobility electron gas present at the $LaAlO_3/SrTiO_3$ interface. Although this system has been heavily studied in the last decade, a great number of question are still unanswered. In order to make progress on the understating of this system, we used different metal cappings to induce a quasi two dimensional electron gas (q2DEG) at low thicknesses of $LaAlO_3$ (<4 uc) and we studied the associated magnetotransport properties. This study will additionally pave the way for future spin injection/detection and spin transport devices.

1.1. The $LaAlO_3/SrTiO_3$ Interface

In 2004, Ohtomo and Hwang discovered that the interface between an insulating $LaAlO_3$ layer and an insulating $SrTiO_3$ substrate shows a metallic behavior [1]. Both materials share a perovskite structure and have a similar a lattice constant of 3.79 Å for $LaAlO_3$ and 3.905 Å for $SrTiO_3$ (Figure 1a), so that an $LaAlO_3$ structure stacked on top of a (001)-oriented $SrTiO_3$ experiences a tensile strain of 3%. Although there are two possible interfaces within the system, LaO/TiO_2 (n-type) and AlO_2/SrO (p-type), we will focus entirely on the first one, being the p-type interface insulating [1–3].

The conducting interface exhibits a metal to superconductor transition at about 200 mK [4] (controllable by gate voltage), magnetism [5], confinement within 7 nm from the interface [6,7] and a strong Rashba spin-orbit interaction [8]. Additionally, a critical thickness of $LaAlO_3$ for conduction exists for 4 uc [9], as shown in Figure 1b. This key component will be discussed in detail in the next chapters.

Although 11 years passed after its discovery, due to the complexity of the materials there is still no theory that perfectly describes the inherent mechanisms for the q2DEG formation in this system, albeit a few scenarios have been proposed.

A first scenario relies on the intrinsic polar discontinuity present in $LaAlO_3/SrTiO_3$ interface. In Figure 2a we see that the planes present in $SrTiO_3$ are both neutral along the (001) direction ($(SrO)^0$ and $(TiO_2)^0$). The planes of $LaAlO_3$ however have an associated charge ($(LaO)^{+1}$ and $(AlO_2)^{-1}$) that will introduce an electric field within each unit cell. An electrostatic potential is then expected between the interface and the top surface. With increasing number of $LaAlO_3$ layers this potential will unfavorably increase and, at 4 uc of $LaAlO_3$, the system goes through electronic reconstruction to avoid a polar catastrophe [3,10,11]. The critical thickness for conduction of 4 uc, represented in Figure 1, can also be explained by this scenario.

At this thickness, the potential introduced by $LaAlO_3$ is large enough for the valence band to be tilted, thus reaching the energy level of the conduction band of $SrTiO_3$, as shown in the band structure of Figure 2b.

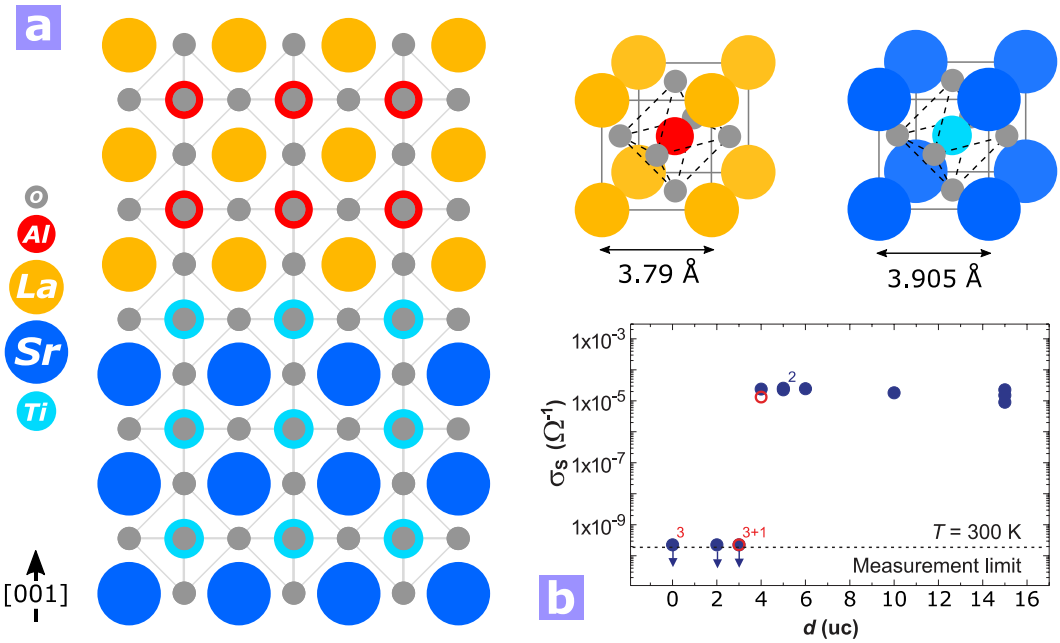

Figure 1 – The metallic $LaAlO_3/SrTiO_3$ interface. a) 2D atomic stacking of $LaAlO_3$ layers over a $SrTiO_3$ substrate in the (001) direction. On the right side, the unit cell (uc) for both materials is represented. **b)** Sheet conductance at room temperature as a function of the number of $LaAlO_3$ unit cells. A clear insulator-metal transition is observed at 4 uc [9].

Since Ti ions at the interface are able to change their valence from +4 to +3, Zener breakdown occurs and electrons may travel into the $SrTiO_3$ and stay confined. This electron transfer generates an opposite electric field that counterbalances the inner potential of the $LaAlO_3$ layer. The field can only be completely canceled for thick $LaAlO_3$, where a transfer of half an electron per uc is expected from the $LaAlO_3$ top layer to the interface, resulting in a (maximum) carrier concentration of 3.3×10^{14} cm^{-2} in the system. Although the extraction of the carrier concentration has to be made with caution (as we will discuss in the chapters ahead), the typical experimental values extracted are around 2×10^{13} cm^{-2}, much lower than predicted by the electronic reconstruction scenario but possibly justified by Anderson localization of interfacial charges and the existence of more than one type of electrons contributing to conduction [10]. It is also debated that the built-in electric field is in fact much weaker than what the polar discontinuity scenario proposes and consequently the band bending will not be enough to pull the $LaAlO_3$ valence band over the $SrTiO_3$ conduction band [12,13].

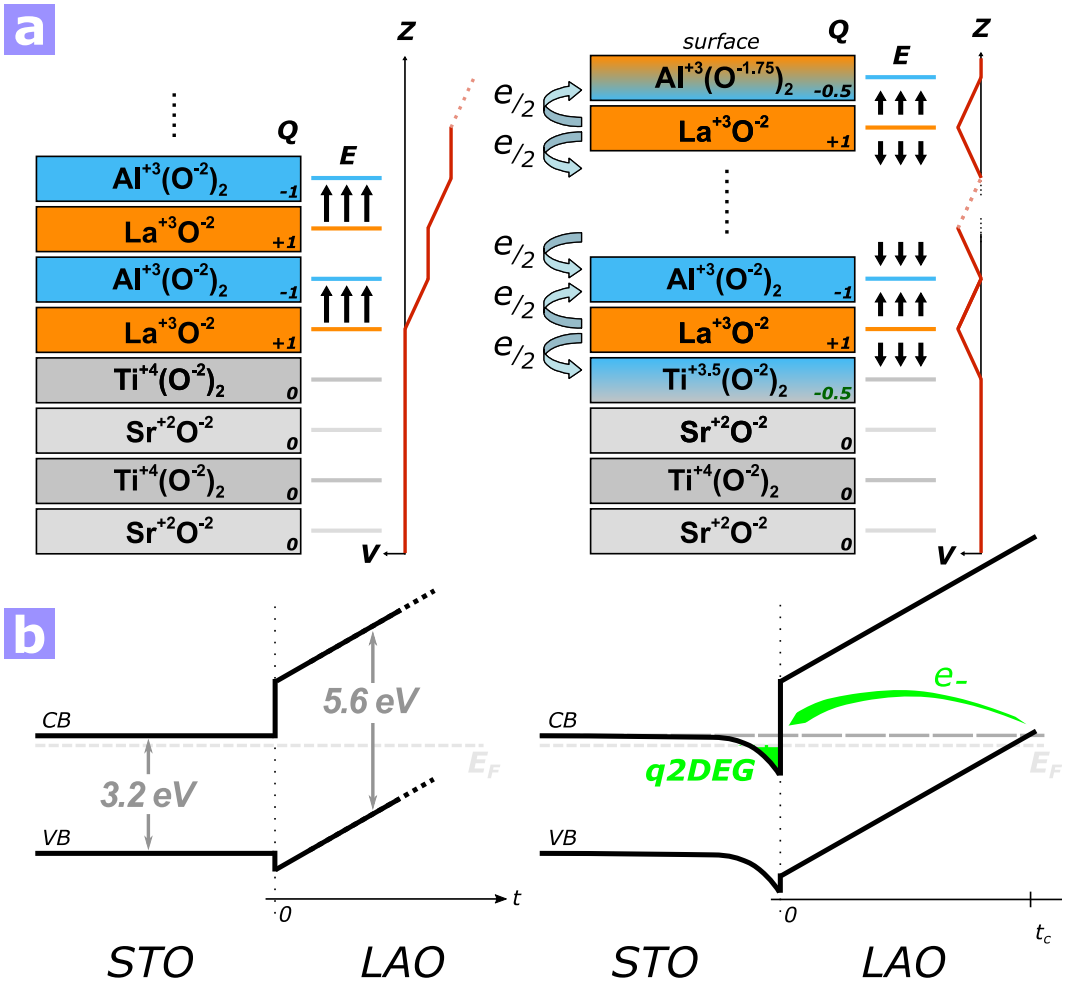

Figure 2 – Electrostatic reconstruction scenario. a) Schematic representation of the polar discontinuity at $LaAlO_3/SrTiO_3$ heterointerfaces. On the left side the unreconstructed n-type LaO/TiO_2 interface. Along the (001) direction $SrTiO_3$ shows neutrally charged planes (Q=0) while $LaAlO_3$ planes have an associated charge of Q=1 and Q=-1. The electrostatic potential V therefore starts building up at the interface and keeps increasing with $LaAlO_3$ film thickness. On the right side a polar catastrophe is avoided through the transfer of half an electron to the TiO_2 interfacial plane. The potential remains finite since the electric field oscillates around E=0 along the (001) direction. **b)** Simplified band structure of $LaAlO_3/SrTiO_3$ interface. The increasing thickness raises the internal potential allowing the $LaAlO_3$ valence band (VB) to shift until it reaches the $SrTiO_3$ conduction band (CB). At this critical thickness t_c, Zener breakdown occurs and electrons are able to travel into Ti 3d states at the interface where the q2DEG appears.

Using a pure electrostatic approach is still not satisfying, which indicates that extrinsic mechanisms may be involved in the formation of the q2DEG.

Since the idea of an atomically abrupt interface is too risky to be considered in a real system, cation intermixing at the interface may indeed form a metallic La-doped $SrTiO_3$ just below the interface, as suggested by some authors [3,14]. This scenario however fails to explain the rigorous critical thickness of $LaAlO_3$ for conduction.

Oxygen vacancies in bulk $SrTiO_3$ could also be a possible explanation, being the $SrTiO_3$ so sensitive to stoichiometric deviations [15,16]. Indeed since the growth of $LaAlO_3$ is made at low oxygen pressures ($P_{O_2} < 10^{-5}$ mbar) a contribution of oxygen vacancies to the total carrier density should be present. A clear influence of the annealing process can be observed in Figure 3a. On the left side we see a sample without annealing, exhibiting a 3D-like conduction that extends throughout $SrTiO_3$ bulk with sheet carrier densities around 10^{17} cm^{-2} at low temperatures. To achieve interfacial conduction (right side) a high temperature annealing in a high oxygen pressure (200 mbar) after growth is required in order to fill oxygen vacancies. This way, the total carrier density decreases to values around 10^{13} cm^{-2} [6,17–20].

In Nakagawa's scenario [3] it is assumed that half an electron is missing from the uppermost AlO_2 layer. According to some authors [21–23] this half electron comes from the ionization of oxygen atoms at the surface of $LaAlO_3$. The creation of donor states at the interface depends on the internal field and consequently on the thickness of the grown film. With the formation of these vacancies, in-gap states will appear close to the conduction band of $LaAlO_3$ and the electrons released are transferred to the interface, reducing the film's electric field and enabling conduction, as shown in Figure 3b. A critical thickness is also expected, directly related with the formation energy of an oxygen vacancy at the surface.

Recently, Yu and Zunger proposed a theoretical polarity-induced defect mechanism that elucidates on the formation, origin and properties of the gas, the insulating p-type interface and the existence of a critical thickness and interface magnetism [24]. The mechanism discards electron reconstruction and justifies the physics in the system with the coexistence between spontaneous formation of surface defects and interfacial cation antisite defects. Increasing $LaAlO_3$ thickness

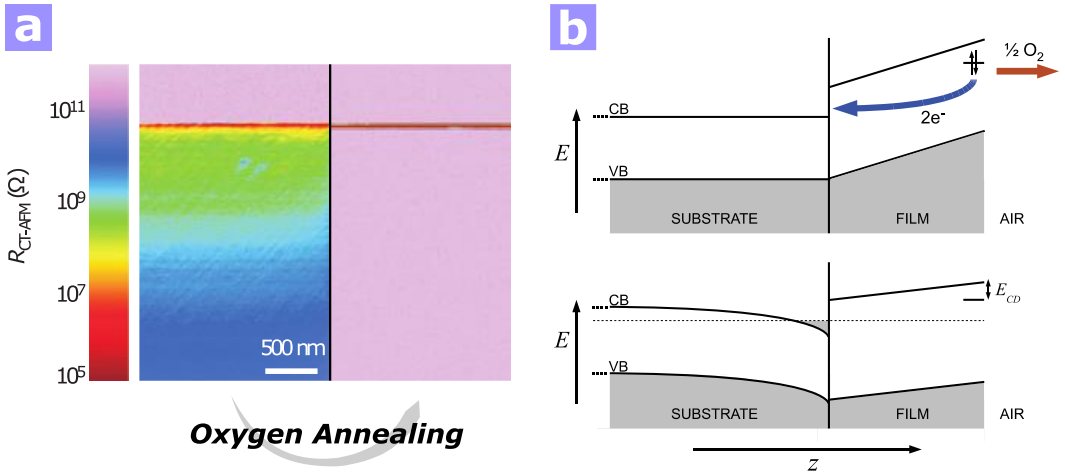

Figure 3 – The role of oxygen vacancies. a) Conductive-tip atomic force microscopy (CT-AFM) resistance mapping around the interface. In the left case conduction spreads in depth through the $SrTiO_3$ substrate most likely due to oxygen vacancies formed during growth process. An oxygen annealing fills these vacancies and interfacial conduction is achieved. (Modified from [6]) **b)** Band diagram of an interface between a polar film and nonpolar substrate. Donor states are created through the appearance of vacancies at the surface leading to electron transfer. The reconstruction also attenuates the film's internal field. (Modified from [21])

leads to an increase of the internal polar field, which will favor thermodynamically the formation of shallow donors and deep acceptor states. This approach however has to be carefully interpreted, since it regards a system in a non-equilibrium state (during growth).

1.2. Devices and Suppression of the Critical Thickness

Aside from the questions left unanswered about the behavior of this system another issue rises. For the use of $LaAlO_3/SrTiO_3$ in spintronic devices, it is of the upmost importance to control the tunnel barrier resistance. Tuning the thickness of the barrier is one solution, but as we saw previously, a minimum of 4 uc of $LaAlO_3$ is imperative for conduction. In [25] the resistance imposed by this thickness, is extremely beneficial for spin injection. Indeed, the conductivity mismatch problem discussed in [26] is inherently solved by the $LaAlO_3$, since it acts as a tunnel barrier [27,28]. The problem here is in terms of spin detection. A drastic reduction of the barrier resistance is required.

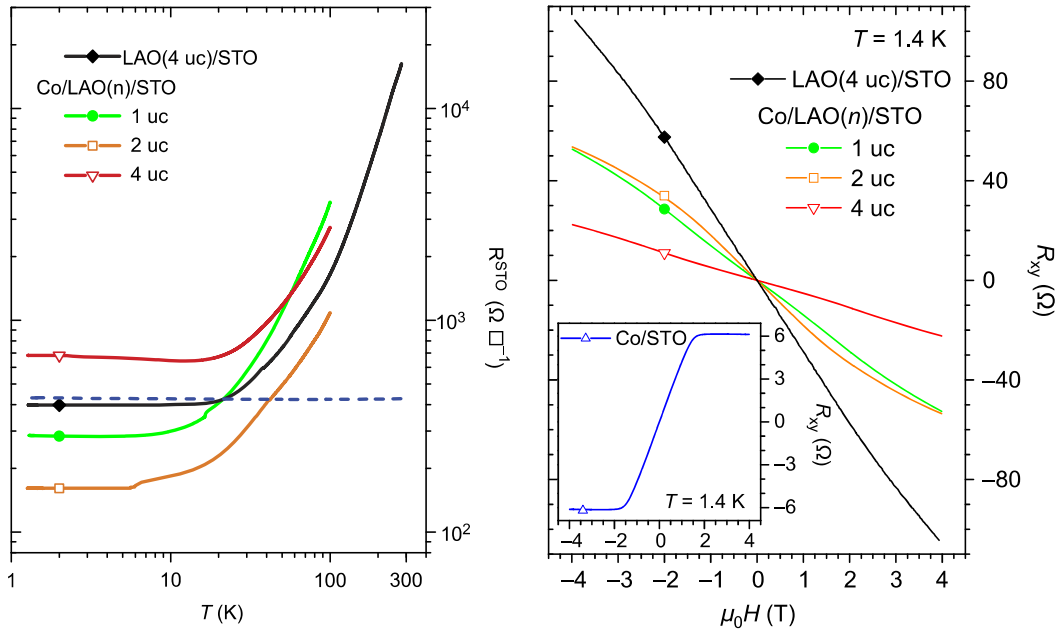

Figure 4 – Co capped $LaAlO_3$ (<4uc)/$SrTiO_3$ transport measurements. Experimental longitudinal sheet resistance and Hall effect measurements for capped structures with different $LaAlO_3$ thicknesses at low temperature. All curves gathered are rather similar to the behavior of a reference $LaAlO_3/SrTiO_3$ with 4 uc (black curved) which proves that a q2DEG can be induced below the 4 uc critical thickness. The inset on the right shows the small contribution of the Co layer for the Hall effect experiments. (Modified from [30])

Density functional theory (DFT) calculations showed that by introducing a metal overlayer on top of $LaAlO_3/SrTiO_3$ structures, the LaAlO3 critical thickness can be suppressed [29]. Taking the example of a Ti capping, besides the appearance of a Schottky barrier between the metal and oxide film, a total attenuation of the internal field in the $LaAlO_3$ and an enhanced carrier concentration in the n-type interface is obtained. For a Fe capping the film shows a similar field, but for other metals like Cu, Ag, or Au the field is large, even larger than in the uncapped $LaAlO_3/SrTiO_3$ in the case of Au. Arras *et al.* [29] also made an analogy between the work function of each metal and the observed calculations, since different metals show their own influence on the electrostatic boundary conditions. Higher work functions might preclude charge transfer to the interface and prevent the formation of the q2DEG.

This critical thickness reduction was experimentally demonstrated in our lab using a Co overlayer [30]. Figure 4 shows a strikingly similar behavior between $LaAlO_3$ (4uc)/$SrTiO_3$ and the Co/$LaAlO_3$ (n)/$SrTiO_3$ with n=1, 2 and 4 uc. Additionally, the carrier concentrations extracted from the Hall measurements are indeed larger[1] than the uncovered structures, just like Arras *et al*. predicted. Nevertheless, in order to viably use the metal has a modulator of the properties of the q2DEG at the interface, further tests and evaluations must be made. In this dissertation we will focus on the magnetotransport of metal/$LaAlO_3$/$SrTiO_3$ (metal: Ti, Ta, Co, Py[2], Pt, Pd and Au) heterostructures. We will also discuss two mechanisms behind the formation of the q2DEG for these types of structures and look at the magnetotransport data gathered.

[1] As we will see ahead, the carrier concentration can be estimated by the slope of the Hall curve at high fields. A smaller slope translates in a higher carrier concentration.

[2] Py designates the $Ni_{80}Fe_{20}$ alloy know as permalloy.

2

Methods

The growth of oxides is a task that involves extremely well defined parameters. Three aspects must be thoroughly investigated in order to have a heterostructures with the desired properties: the substrate, the target and the growth conditions. For this work, (001)-oriented $SrTiO_3$ substrates with TiO_2 termination from *CrysTec GmbH* were used. The 7 x 7 mm^2 substrates are terminated (with a miscut of 0.05°– 0.1°) by *Crystec*, shipped to the lab and then cutted by us with Diamond Wire Saw Cutting in four 3 x 3 mm pieces. The termination is then investigated with atomic force microscope (AFM) before starting the growth. A quality check was additionally done in between each process[3]. Also, $SrTiO_3$ substrates were at first terminated by us, following the Kawasaki method [31], which led to identical topography and transport properties as the ones terminated by *Crystec.*

In order to grow the $LaAlO_3$ layer we used pulsed laser deposition (PLD) as it is the preferred technique to grow high quality oxide structures. A schematic of the process can be seen in Figure 5a. A single crystal of $LaAlO_3$ was ablated by a KrF (248 nm) excimer laser at a repetition rate of 1 Hz and with a fluence of 0.7 J/cm^2. The laser passes through a slit, which defines its beam size. The beam is guided though deflecting mirrors, focused on the target with two converging

[3] For the heterostructures, the metal deposition is made in-situ with a connected sputtering chamber, which prevents us from checking the quality with AFM between growths. Nevertheless, $LaAlO_3/SrTiO_3$ without metal were extensively investigated before stepping onto the metal heterostructures, to ensure that the PLD step was producing high quality samples.

lenses and then passes through a quartz window before reaching the target. The energy was tuned with a regulated attenuator placed between the slit and the lenses making the energy that reaches the target variable, while maintaining a laser source voltage constant at 21 kV. It is also worth mentioning that the energy was measured using an energy sensor placed between the converging lenses and the quartz window[4]. A sketch of the optical path is shown in Figure 5b. During ablation the target was rotated in an inward circular like motion to avoid melting and subsequent change of the target stoichiometry. Moreover, the target was polished with sandpaper and pre-ablated at a laser fluence of 1 J/cm^2 at a repetition rate of 5 Hz for a total of 20000 pulses. The background pressure was kept at 2×10^{-4} mbar of oxygen. This process was done every 20 growths to ensure a good surface for ablation.

The TiO_2 terminated substrates, glued to a substrate holder using silver epoxy, were kept at 730 °C under a partial oxygen pressure of 2×10^{-4} mbar and with a substrate-to-target distance of 5 cm. The layer-by-layer growth allows us to have a precise control over the $LaAlO_3$ thickness through real-time monitoring of reflection high-energy electron diffraction (RHEED) intensity oscillations. An electron gun generates a beam (30 kV) that irradiates the surface of the target at an incident angle of 1-2º . Reflected electrons are collected with a phosphor screen and imaged by a CCD camera. In Figure 5c we can see the layer by layer growth of samples with different $LaAlO_3$ thicknesses.

The intensity starts dropping when the first species arrive at the substrate and as they form a new layer of material the signal gets back (or close) to the initial intensity (further explanation in Annex 1 – Growth Modes). Therefore, each peak represents exactly one unit cell grown, with around 20 pulses required per unit cell (for the fluence previously mentioned). After the desired thickness is achieved the temperature of the sample is lowered to 550 °C at a rate of 20 °C/min. and put at a pressure of 0.1 mbar of O_2.

[4] This measured energy does not take into account the attenuation imposed by the quartz window. Since this window is in contact with the deposition chamber, it will eventually get "dirty" over time. A fluence of 0.7 J/cm^2 enabled good $LaAlO_3/SrTiO_3$ samples for a clean window (97% transmission) but the transmission can get down to 70% with a few tens of deposition processes. Regarding this issue, the window was cleaned regularly, or a generic $LaAlO_3/SrTiO_3$ sample was made from time to time, in order to adjust the energy required to make a good sample.

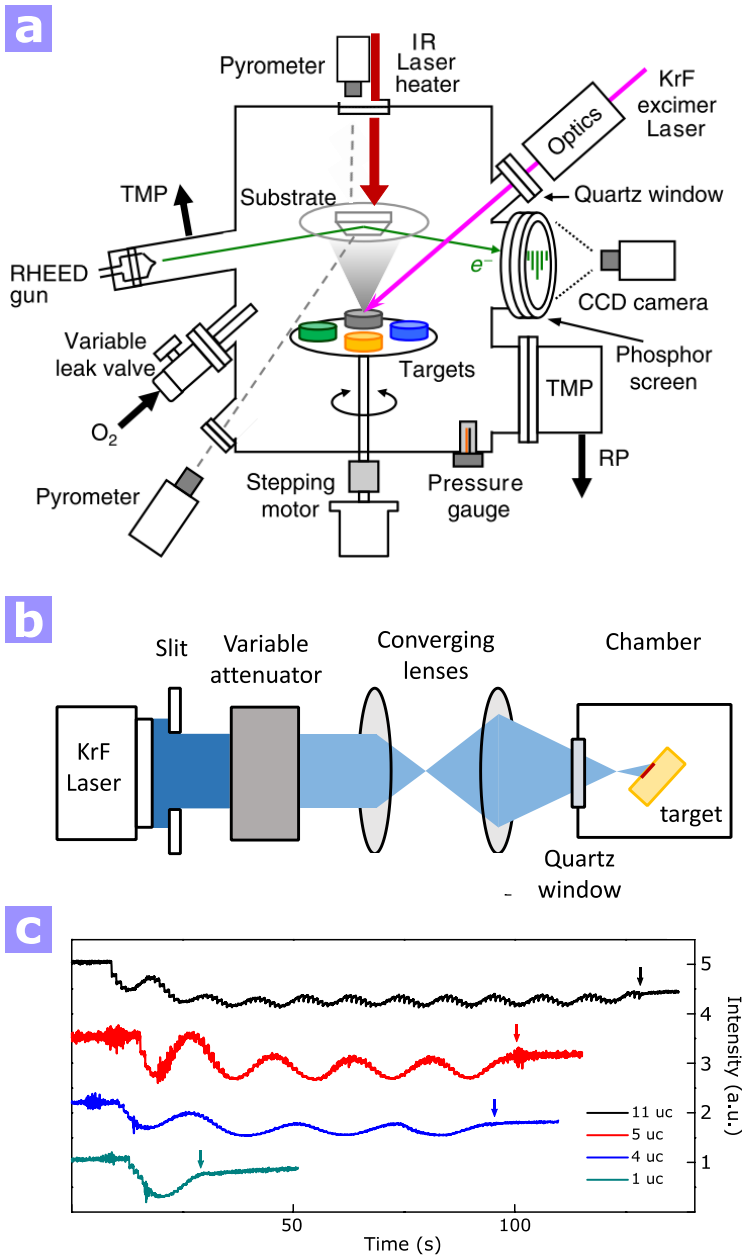

Figure 5 – Experimental PLD system. a) Schematic illustrating the PLD system used. Four different targets are available inside the chamber. The KrF excimer laser shoots the desired target, creating a plume of material to be deposited. The substrate holder is heated with an infrared laser and the temperature is measured by two pyrometers (one on the top and another on the bottom measuring the sample directly). The turbomolecular pump (TMP) and rough pump (RP) allow a vacuum inside the chamber of around 10^{-9} mbar. **b)** The beam geometry is firstly defined by a slit. It goes through a variable attenuator and an optical stage composed by two converging lenses (focal lengths f_{o1}=100 mm and f_{o2}=150 mm) to define the spot size. Additional deflecting mirrors for beam guidance are not shown for clarity [64]. **c)** Typical time dependent RHEED intensity oscillations. Each peak represent one monolayer deposited.

The samples are then annealed at 550 °C for 60 min at a partial oxygen pressure of 200 mbar, to fill oxygen vacancies (as suggested in [9]). Finally, they were cooled down at 25 °C/min, at the same pressure, until they reach room temperature.

Several samples of 5 and 10 uc were made to ensure that a q2DEG was present in all of them. After growth, the room temperature sheet resistance of each sample was checked using four-wire van der Pauw configuration. As we will see ahead the values achieved were around 100 kΩ/□, indicating good sample quality.

With the process optimized, 1 and 2 uc structures were made for metal deposition. Magnetron sputtering was used to deposit different metals. This process was made *in-situ* and right after PLD to prevent contaminants in between the $LaAlO_3$ and the metal layer. The specific deposition parameters, like partial chamber pressure, power and excitation current had to be changed for each metal, depending on their wetness and adhesion on the $LaAlO_3$ surface.

Additionally, $SrTiO_3$ substrates were carried through the whole cycle described (skipping the laser shooting and the metal deposition) to ensure that an observed conductive interface was not due to doping of the substrates during the growth process. All $SrTiO_3$ substrates measured after this test were insulating.

The samples were contacted with aluminum wire using ultrasonic wire wedge bonding in four-wire van der Pauw and Hall configuration. The magnetotransport properties of the heterostructures were measured with Quantum Design's Physical Property Measurement System (PPMS) Dynacool with temperature ranging from 300 to 2 K and magnetic fields ranging from 0 to 9 T. The measured raw curves were antisymmetrized accordingly to the method described in Annex 2 – Antisymmetrization and Symmetrization Method, to avoid unwanted contribution of potential misalignment of the contacts during bonding.

Additional pictures of the experimental setup are shown in Annex 3 – Experimental Setup.

3

Results and Analysis

We performed topographical and magnetotransport experiments on $LaAlO_3/SrTiO_3$ samples and metal/$LaAlO_3/SrTiO_3$ using different metals. Atomic force microscopy (AFM) was used to analyze surface morphology, to ensure good growth and deposition quality. The transport data was analyzed using van der Pauw method and Hall effect in order to give further insight on the behavior of the q2DEG at a wide range of temperature and magnetic fields and for different electrostatic boundary conditions induced by a top layer. The strong spin-orbit interaction known to be present in the q2DEG is also taken into account. A comparison is made between structures with different capping layers and two mechanism are proposed regarding the formation of the q2DEG.

3.1. Surface Morphology

Structural quality is one of the most essential steps to achieve quality $LaAlO_3/SrTiO_3$ interfaces. Given the sensibility of conditions for the formation of a q2DEG, making sure that the growth process leads to high quality surfaces is a challenge. Fortunately vast theoretical and experimental studies have been carried in the past, which enables us to save a lot of time. We will therefore not focus on the variation and consequences of these conditions, but rather on the analysis of the good samples.

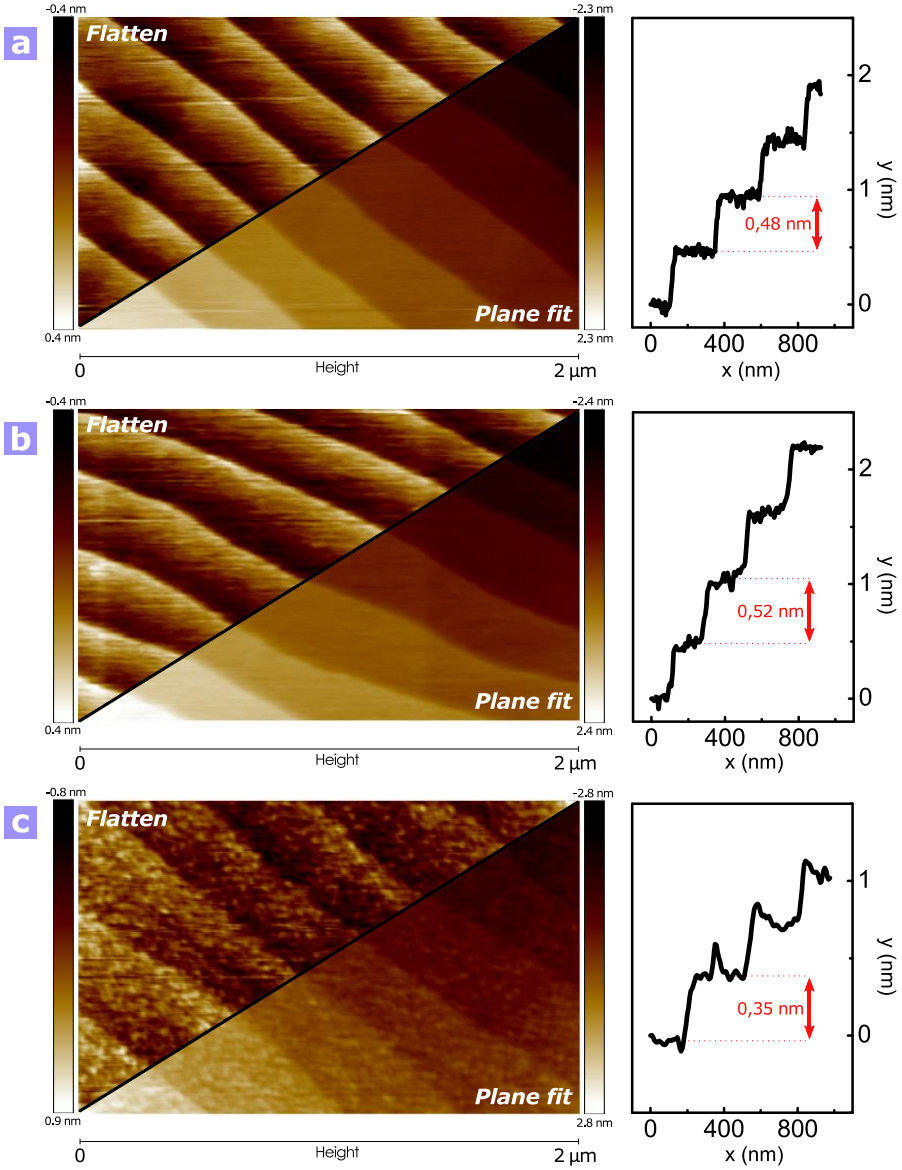

Figure 6 - Surface morphology analysis using AFM with both flatten and plane fit treatment. a) Bare TiO_2 terminated $SrTiO_3$ as received from *Crystec*. **b)** $LaAlO_3$ (4uc)/$SrTiO_3$ **c)** AlO_x/Py/$LaAlO_3$ (1uc)/$SrTiO_3$. The Al was used to protect the Py layer and most likely takes the form of AlO_x due to surface oxidization.

We have performed a brief AFM topography study of TiO_2 terminated $SrTiO_3$ substrates, $LaAlO_3/SrTiO_3$ and metal/$LaAlO_3/SrTiO_3$ heterostructures. On the left side of Figure 6 we show the topography of each of these structures. Each image was split in two different post acquisition processes, the first one being a flattening and the second a plane fit. These treatments are usually done in

order to remove background "bow" and "tilt" due to the movement of the tip. On the right side we plotted the height progression (y), slicing the plane fit image (x).

Starting with the bare $SrTiO_3$, a good surface with step terrace is shown (Figure 6a). The step has an approximate height of 0.48 nm which is fairly similar to the 0.39 nm lattice parameter for $SrTiO_3$ (see fig. 1). We estimated the root mean square surface roughness value (R_q) averaging over three 2 x 1 μm images from different locations across the sample. For the bare $SrTiO_3$ we obtained $R_q = 0.70$ Å. These surface roughness values are in fact mainly dominated by the steps and terraces of the substrate. The scan done after a $LaAlO_3$ growth is shown in Figure 6b. The roughness $R_q = 0.81$ Å is quite similar to the one obtained previously. This suggests smooth and continuous full coverage of the $LaAlO_3$ layer grown. Moreover, both the surface topography and the step height are very similar to the former. Lastly, we look at AlO_x/Py/$LaAlO_3$ (1uc)/$SrTiO_3$. We should first note that this sample does not come from a metal deposition on the $LaAlO_3$/$SrTiO_3$ analyzed in Figure 6b (check footnote 3). Nevertheless we similarly extracted $R_q = 1.56$ Å. It is also important to note that the metal tends to oxidize over time. The sample shown in Figure 6c was measured one month after metal deposition. The AFM image shows a slight formation of what possibly is aluminum oxide which might explain the increasing roughness. The characteristic step terrace surface of the underlying $LaAlO_3$ is however still clearly visible, which demonstrates a uniform metal deposition.

Additionally, a sketch of the step terrace surface is displayed in Figure 7a for a clearer understating of the analysis done above.

As mentioned in Methods, RHEED was used to track real time the growth evolution. The plot shown in Figure 5c comes from the intensity of the RHEED patterns obtained by the diffraction of electrons in the sample structure. Patterns are shown for the three different structures. Since the main point of this dissertation is not the study of $LaAlO_3$ growth, will not go too deep into the study of these patterns. However, we can see that for both $SrTiO_3$ and $LaAlO_3$/$SrTiO_3$, sharp Bragg diffraction rods and Kikuchi lines are observed, which is indicative of a high crystalline quality. For a metal capping on top of $LaAlO_3$/$SrTiO_3$ the pattern changes radically. The diffraction ring pattern observed is typically

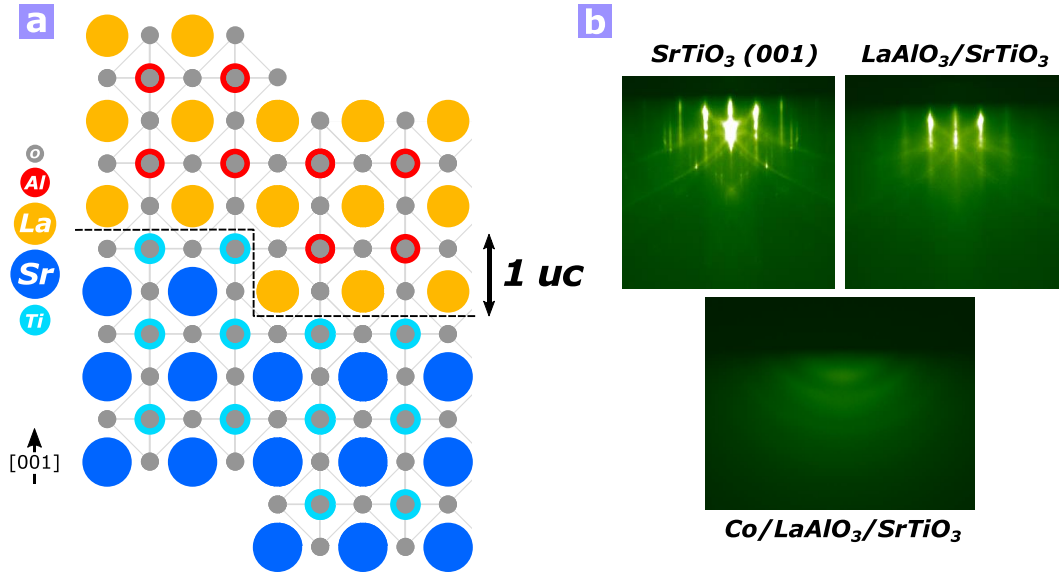

Figure 7 - Miscut and RHEED patterns. a) Schematic exemplifying the step terrace morphology observed in Figure 6. b) Different RHEED patterns from electron diffraction to demonstrate the progression of crystalline quality with the $LaAlO_3$ and metal deposition.

seen for polycrystalline films, where there is no preferential orientation.

3.2. *Transport Properties*

3.2.1. *Van der Pauw Method*

The van der Pauw method has been used for the last fifty years to accurately measure the electrical properties of samples with any arbitrary shape. Through these measurements, physical properties such as the doping type, sheet carrier density and sheet resistance can be determined. As a requirement, the sample must have uniform thickness, homogeneous composition and isotropic electrical properties. The contacts must be placed on the perimeter of the structure and be much smaller than the whole area measured. The schematic on the left side of Figure 8 shows the four-point van der Pauw configuration used in our samples. A current I is applied through contacts a and b and a voltage drop V is measured between contacts d and c, which results in a resistance given by:

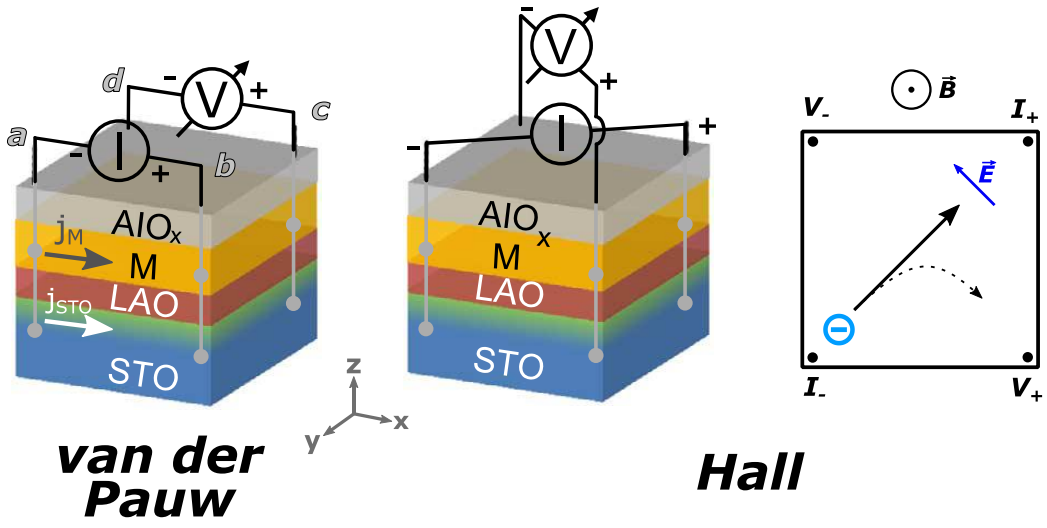

Figure 8 - Schematic of the connection in van der Pauw and Hall configuration. The aluminum wire is buried deep in the heterostrucure so that two current density are measured: j_M and j_{STO}, contributions from the metal and q2DEG respectively. An additional schematic from the top view of the Hall effect (right side) demonstrates the deviation of injected electrons due to an electric field E generated by the application of an out-of-plane magnetic field B.

$$R_{ab,dc} = \frac{V_{dc}}{I_{ab}} \tag{1}$$

Since $R_{ab,cd} = R_{cd,ab}$ accordingly to the reciprocity theorem (interchangeable current/voltage contacts), average values for $R_{xx} = (R_{ab,cd} + R_{ba,dc})/2$ and $R_{yy} = (R_{ad,cb} + R_{da,bc})/2$ can be determined. From [32] we can represent the resistivity ρ as:

$$\rho = \frac{\pi d}{\ln(2)} \frac{R_{xx} + R_{yy}}{2} f \tag{2}$$

where d is the thickness of the sample and f is the van der Pauw correction factor that relates with the ratio R_{xx}/R_{yy}. Since the samples have a square shape and the bonding is done in the corners, we assume that $R_{xx} \approx R_{yy}$, within a few percentage of error. Therefore, $f \approx 1$ and eq. (2) can be reduced to:

$$R_s = R_{xx} \frac{\pi}{\ln(2)} \tag{3}$$

where R_s ($\Omega/\square$) represents the ratio ρ/d for a two-dimensional electron gas of unknown thickness.

3.2.2. Hall Effect

When an out-of-plane magnetic field $\boldsymbol{B}$ is applied to a conductor, charged particles in motion will be deflected. This phenomenon can be described in a semi-classical approach with a Lorentz force $\boldsymbol{F}$ given by:

$$\boldsymbol{F} = q(\boldsymbol{E} + \boldsymbol{v} \times \boldsymbol{B}) \tag{4}$$

where q and v are the charge and velocity of the carriers and $\boldsymbol{E}$ is the electric field. On the right side of Figure 8 a top-view scheme illustrates an applied current between $I^+$and I^- where the trajectory of electrons is bended due to $\boldsymbol{B}$, and a voltage between $V_H^+$and V_H^- develops.

For a 2D conductor the resistance is dimensionally equivalent to a resistivity for an unknown thickness, so that the transverse resistivity can be written as:

$$\rho_{xy}^{2D} = \rho_{xy}^{3D}.d = \frac{V_H^- - V_H^+}{I^- - I^+} = R_{xy}^{sheet} \tag{5}$$

The current density induced by an electric field perpendicular to an applied uniform magnetic field can be expressed by Ohm's law as:

$$\underline{\underline{\boldsymbol{\rho}}}\boldsymbol{j} = \boldsymbol{E} \tag{6}$$

where the tensor of resistivity has the form of:

$$\underline{\underline{\boldsymbol{\rho}}} = \begin{pmatrix} \rho & -R_H B \\ R_H B & \rho \end{pmatrix} \tag{7}$$

Since the Hall coefficient is given by $R_H = -1/nq$, where n is the total charge carrier concentration, the transverse resistance of the q2DEG only can be written in terms of the q2DEG charge carrier density n_S and the current I_* that flows in the q2DEG as:

$$R_{xy}^* = -\frac{B}{n_S q} = \frac{V_H}{I_*} \tag{8}$$

With $V_H = R_{xy} I_T$ (subscript T meaning total = q2DEG + metal contribution) and knowing I_T and I_*, n_S given in cm^{-2}, can be written as:

$$n_S = \frac{I_*}{R_H q I_T} \tag{9}$$

where $R_H = -R_{xy}/B$ and is equivalent[5] to the slope obtained from a linear fit to the transverse magnetoresistance $R_{xy}(B)$. A positive n_S comes from a negative slope of the curve and corresponds to electron-based conduction.

Additionally, from Drude formula the conductivity comes:

$$\sigma_{xx}^{3D} = \frac{1}{\rho_{xx}^{3D}} = q d \mu_H n^{3D} \tag{10}$$

Again, since we are dealing with a 2D conductor, $n^{3D} \Leftrightarrow n^{2D}$. Finally, the Hall mobility μ_H, given in $\mathrm{cm}^2/(\mathrm{V.s})$, can be written as:

$$\mu_H = \frac{1}{q R_s n^{2D}} \tag{11}$$

3.2.3. Quantum Corrections

Although the semi-classical approach is able to provide us reasonable insights, dealing with two dimensional systems at low temperatures requires also a quantum mechanical approach.

For an electron traveling in a disordered system closed time reversed paths have to be considered, due to elastic scattering events. Constructive interference between pairs of these paths will increase the probability to find a particle at a given position and time, thus enhancing localization. This phenomenon is called weak-localization (WL) and will eventually lead to a quantum reduction of conductance. An external magnetic field is expected to suppress weak-localization,

[5] This equivalence is valid when only one type of carrier contributes for conduction. As we will see ahead, the complexity increases when multiple carriers populating different bands are considered.

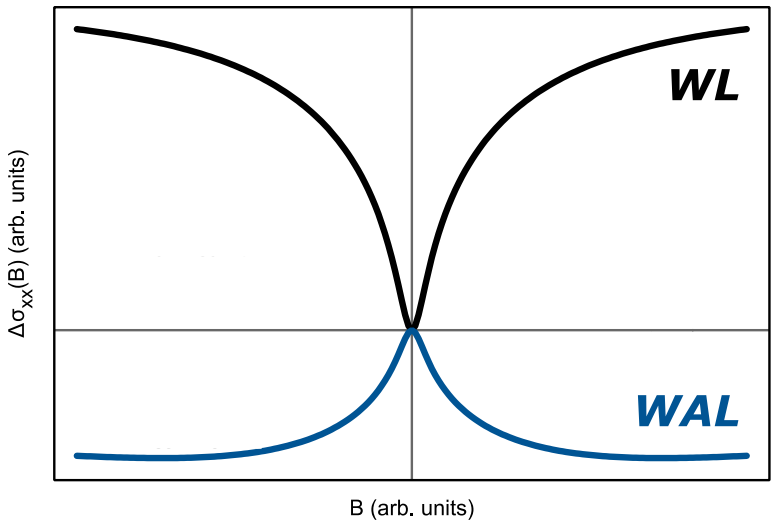

Figure 9 - Theoretical magnetoconductance curves in the weak localization (black) and weak antilocalization regime (blue) [65].

since it will break time-reversal symmetry, and conductance increases. However, in the presence of spin-orbit coupling[6], the spin of the electron cannot be neglected. Along two time-reversal paths the electron will suffer opposite spin rotation, and ultimately, destructive interference between these two events reduce the probability to find the electron, and conductance increases. This is known has weak-antilocalization (WAL). Yet again, the presence of an external magnetic field will preferentially influence the spin rotation mechanism. The WAL positive contribution is suppressed and therefore magnetoconductance decreases. The effect of both WL and WAL on the magnetoconductance is displayed in Figure 9.

3.2.4. Band Structure and Spin-Orbit Interaction

As mentioned before, Ti atoms in the system will be able to host electrons in their 3d conduction band. In the schematic of Figure 10a we consider Ti atoms in cubic $SrTiO_3$ where the quintuplet of states of an isolated Ti atom breaks into a two-fold e_g and three-fold t_{2g} set. In bulk, the three t_{2g} bands have an ellipsoidal Fermi surface and are centered at the Γ point. At the $LaAlO_3/SrTiO_3$ interface

[6] Spin-orbit coupling can be seen as an additional contribution to the Hamiltonian of the system that describes the interaction between the particle spin and its motion.

the degeneracy is lifted due to tetragonal distortion and broken inversion symmetry. The d_{xy} band is therefore shifted to a lower energy relative to the $d_{xz/yz}$ bands [33], as we can see in Figure 10b. For lower carrier densities, we can conclude that all electrons are expected to reside in the d_{xy} band and only one type of carries is present in the system. With increasing carrier density the $d_{xz/yz}$ bands are populated and conduction is expected to be held by multiple types of carriers. It is important to notice here how the transport analysis regarding a single band model is insufficient to describe the system at high carrier densities although it might give us a glimpse of some basic electronic features. This point will be addressed in the next section.

Yet again, adding spin-orbit interactions (SOI) furthers increases the complexity. In [34], it is discussed that most spin-orbit effects in the system come from atomic spin-orbit (ASO) coupling. From Figure 10c, the main effect of ASO to the band structure is the band mixing at the Γ point seen in the bottom of the $d_{xz/yz}$ bands. Since the Rashba SOI present in the system is closely connected with ASO interaction, the Rashba SOI strength will also peak at the bottom of $d_{xz/yz}$ bands, as seen in Figure 10d. It is worth to say that the large SOI existing within the q2DEG at $LaAlO_3/SrTiO_3$ interface originates from either or both the Rashba SOI [35,36] and ASO interaction [34].

Interestingly, an external gate voltage will let us sweep a wide range of energies. From modulation of transport properties achieved by Caviglia *et al*. (represented in Figure 10e) we notice that a positive gate voltage will result in an accumulation of electrons at the interface and a subsequent increase of the carrier concentration and overall energy (WAL regime). For negative gate voltage there is a reduction in energy and carrier concentration drops (WL regime). Field effect modulation of the q2DEG has been extensively investigated by other authors in the past as a powerful way to tune the electron doping level in the system [8,34,36–39]. A relation can therefore be acquired between the WL and WAL regimes and the SOI strength. We can conclude that when the carrier concentration is low, a WL regime is expected as well as a low SOI strength. As the carrier concentration increases, we enter the WAL regime where a peak of SOI strength

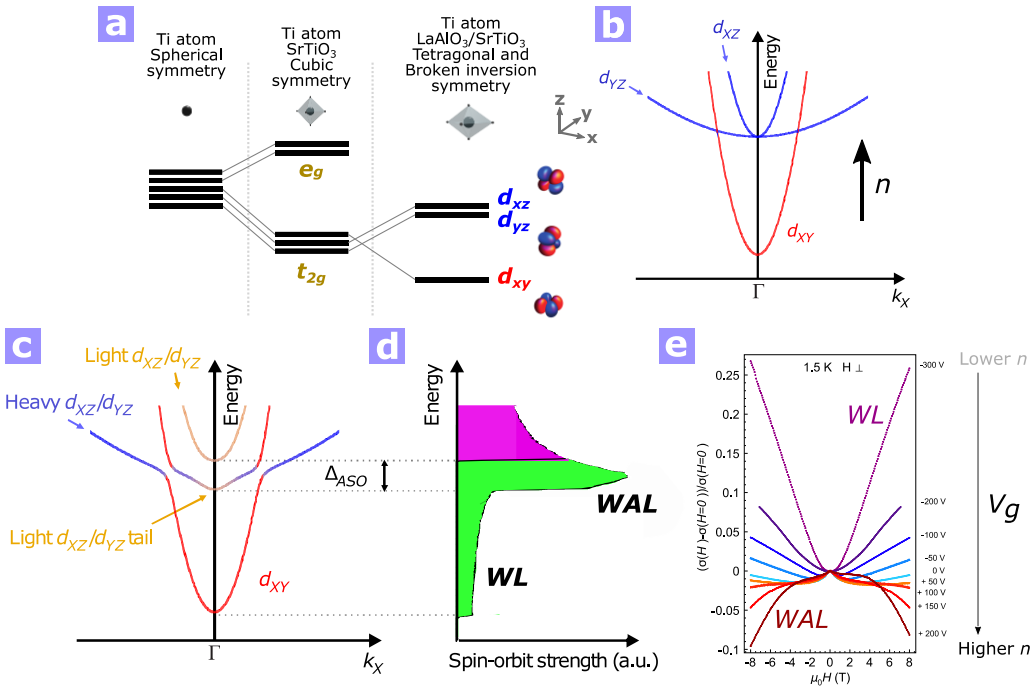

Figure 10 - Band structure and spin-orbit interaction. a) Energy levels of the Ti 3d orbitals in spherical, cubic, tetragonal and non-inverted symmetry. The cubic to tetragonal transition distorts the TiO_6 octahedra and lifts degeneracy of the eg and t_{2g} multiplets. The inverted symmetry in the system leads to completely modified e_g and t_{2g} multiplets due to the confining potential created with interface formation. Specific values taken from x-ray absorption spectroscopy for the amplitude of the splitting can be found in [33]**. b)** Interfacial d-orbital energy bands of $LaAlO_3/SrTiO_3$ aligned at the Γ point. As shown in a) the d_{xy} is lower in energy than the d_{xz} and d_{yz} bands. **c)** Band mixing caused by ASO interaction at the bottom of d_{xz} and d_{yz} bands. **d)** ASO strenght along the Fermi surface. The green area represent the first two bands (d_{xy} and heavy d_{xz}/d_{yz}) while the purple represents the third band (light d_{xz}/d_{yz}). Modified from [34]. **e)** Modulation of the magnetoconductance of $LaAlO_3/SrTiO_3$ interface at low temperatures and under external electric and magnetic field. Modified from [35].

is observed (when $d_{xz/yz}$ bands begin to be populated). Further increase of the carrier concentration might eventually lead to a regime that Fête *et al.* calls Anomalous Metal [39]. As we will see ahead it is indeed possible that the metal capped structures are in this regime, since a higher carrier concentration is expected for this specific system [29].

3.2.5. Results of Magnetotransport Experiments

3.2.5.1. $LaAlO_3/SrTiO_3$ Heterostructures

Before stepping onto the metal capped heterostructures a brief overview of $LaAlO_3/SrTiO_3$ samples with more than 4 uc should be made. In Figure 11 we display the analysis of a 5 uc $LaAlO_3/SrTiO_3$ sample, grown at 730 °C with a fluence of 0.7 J/cm² at a partial oxygen pressure of 2×10^{-4} mbar (with the recommended post annealing at 200 mbar of O_2 and 550 °C to ensure the filling of oxygen vacancies).

The sheet resistance, calculated using eq. (3), is represented in Figure 11a. A reduction of about two orders of magnitude is observed, which indicates metallic behavior, with a low temperature resistance of ~70 Ω/□, a value that goes along with what is found in the literature for a q2DEG in this system. The data showed only reflects measured values during cooling, however, similar results were obtained when measuring in the warming procedure. In Figure 11b we plot the Hall magnetoresistance at 2 K with magnetic fields in the range of 9 T. Although there is a slight non linearity observed, since we are dealing with carrier concentrations of about 3×10^{13} cm^{-2} we assume that carriers in the d_{xy} band dominate the transport readings. We are then in conditions to use the equations obtained in 3.2.1 and 3.2.2. We start by extracting the dependence of carrier concentration over temperature. n_S for each temperature is calculated with eq. (9) where $\frac{I_*}{I_T} = 1$ (all current going to the q2DEG) and R_H equals the slope of the Hall trace for high magnetic fields. As we will see ahead this consideration will be of extreme importance for a correct extraction of the carrier concentration in the system. Contrary to the great dependence of the sheet resistance with temperature, the same dependence is not observed in the carrier concentration, as observed in Figure 11c. A weak dependence with temperature is only observable between 100 K and 300 K. The variation in sheet resistance is in fact due to an increase of electron mobility for lower temperatures, as we will discuss ahead, and possibly due to the cubic to tetragonal transition around 105 K in bulk $SrTiO_3$, which is known to lift orbital degeneracy (see Figure 10a). We additionally display in the inset of Figure 11b the longitudinal magnetoresistance:

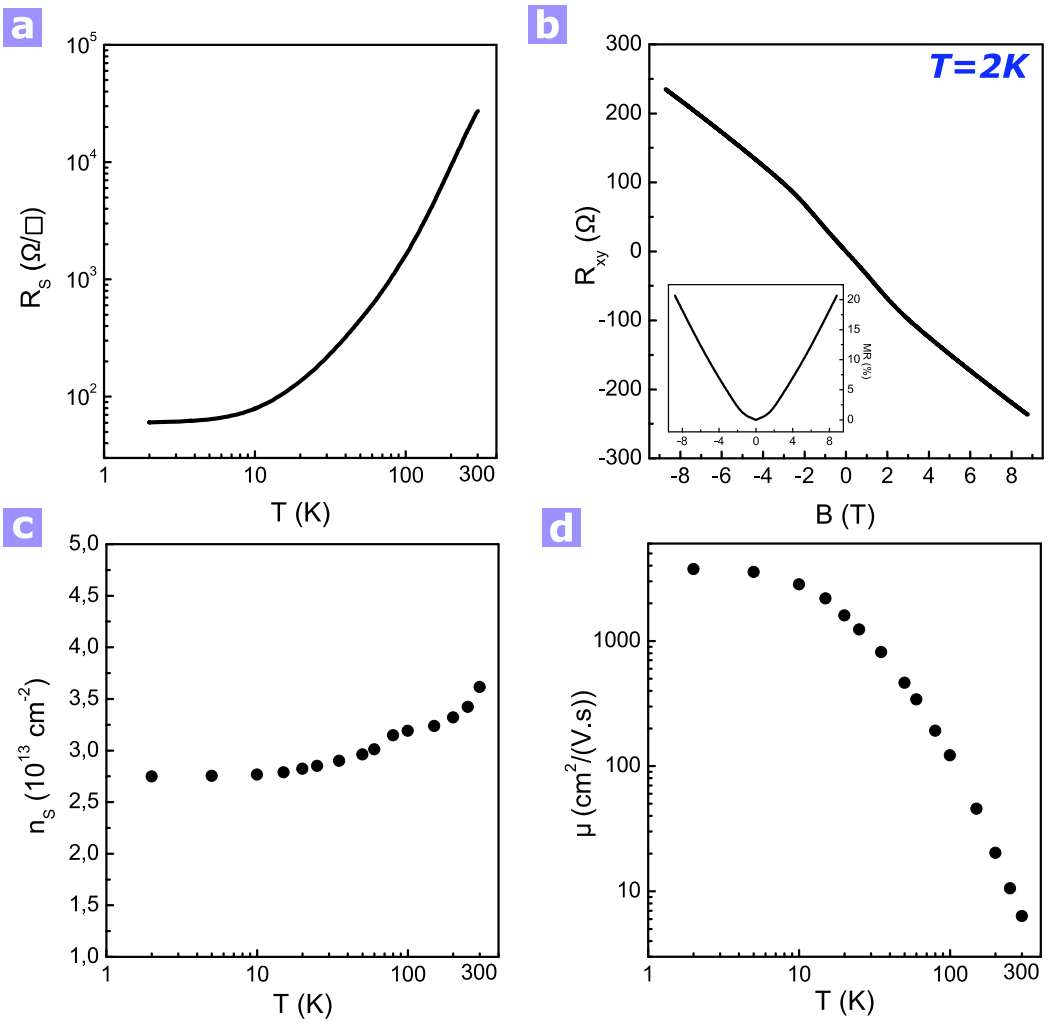

Figure 11 - Transport properties of a $LaAlO_3$ (5uc)/$SrTiO_3$ sample. a) Sheet resistance as a function of temperature. **b)** Hall trace and magnetoresistance (inset) at 2 K for an external out-of-plane magnetic field of 9 T to -9 T. **c)** Sheet carrier concentration as a function of temperature taken from the high field regime slope of Hall experiments (from 2 K to 300 K). Although the uncertainties are not shown they are less than 1% (error associated with the linear fitting at high fields). **d)** Carrier mobilities as a function of temperature.

$$MR = \frac{R_{xx}(B) - R_{xx}(0)}{R_{xx}(0)} \tag{12}$$

We achieved an MR of about 20% for 9 T magnetic fields at low temperatures, values that are again along the ones seen in the literature for similar $LaAlO_3/SrTiO_3$ samples.

The carrier concentration achieved is much lower than the 3.3×10^{14} cm^{-2} predicted by the polar catastrophe model. This discrepancy has been ascribed to

carrier localization due to charge trapping by defect states. Hall measurements will not take into account carriers that are not contributing to conduction. Only mobile carriers are considered, which might explain the low carrier concentration observed. We should also note that the measured carrier densities vary from sample to sample (approximately from 10^{13} to 5×10^{13} cm^{-2}). Using only RHEED as the thickness probing technique might lead to two 5 uc samples with different thicknesses. Additionally, since samples are taken from vacuum to be measured, and some of them stay stored in boxes for long periods for time, adsorbates at the $LaAlO_3$ surface may also incite electrostatic doping.

The temperature evolution of the q2DEG mobility is displayed in Figure 11d. Values range from 5 $cm^2/(V.s)$ at high temperatures to 4000 $cm^2/(V.s)$ at 2 K. This high temperature dependence might be attributed to fundamental behavior of $SrTiO_3$ crystals. Increasing phonon-electron scattering is expected with increasing temperature, which ultimately results in a decrease of electron mobility. On the other hand, the low temperature mobilities are suspected to be reduced by impurity scattering. This problem can be lessen with better interface crystalline quality, mainly controllable by taking more carefully into account the $SrTiO_3$ substrate termination and how good is the arrival of the initial species at the substrate. Finally, given the huge temperature dependence of the dielectric constant of bulk $SrTiO_3$ (four orders of magnitude), the potential well where mobile carriers evolve may also change. Although the internal electric field observed in the system is known to damp the dielectric constant [40], the effects on the band structure should also be taken into consideration.

3.2.5.2. Metal/$LaAlO_3$/$SrTiO_3$ Heterostructures

With the analysis above we conclude that our samples show a q2DEG with properties very similar to the ones described in the literature. A good platform can now safely be used to further analyze the behavior of $LaAlO_3$ (n<4 uc)/$SrTiO_3$ structure with different metal capping layers.

An unpatterned layer of four different metals (Ti, Ta, Co and Py) was deposited by magnetron sputtering, as described in Methods, and then connected with aluminum wire by ultrasonic wire wedge bonding. Due to the stacking of different materials the wire will go through the heterostructures (that only has a few nm until it reaches the $SrTiO_3$). As expected, the measurements done will

include the contribution of both conductive paths, one through the q2DEG and the other through the metal. In order to isolate the gas contribution a simple parallel resistance model gives the evolution of the resistance in the gas with temperature (R_{xx}^{q2DEG}), taking into account the resistance of the metal contribution (R_{xx}^{M}) and the total resistance measured (R_{xx}^{meas}):

$$R_{xx}^{q2DEG}(T) = \frac{R_{xx}^{M}(T) \cdot R_{xx}^{meas}(T)}{R_{xx}^{M}(T) - R_{xx}^{meas}(T)} \tag{13}$$

The preferred procedure to extract the metal contribution $R_{xx}^{M}(T)$ with temperature is to fabricate metal/$SrTiO_3$, metal/$LaAlO_3$ or even metal/SiO_2 heterostructures and measure the longitudinal transport properties[7]. Unfortunately, these samples were not grown along with the samples analyzed ahead. To preserve a consistency between the metal thickness of metal/$SrTiO_3$ and respective metal/$LaAlO_3$/$SrTiO_3$ the samples should be made consecutively. Due to time constrains, repeating the whole set of samples turned out to be impossible during this master's dissertation. However, in [30] the Co/$SrTiO_3$ sheet resistance shows almost no variation with temperature. Although it might be risky to generalize this occurrence for all the metals used here, the variation over temperature will hardly be in the variation range of the q2DEG (two order of magnitude against a few tens of ohms). We will then make two assumptions in our analysis regarding this matter. Since the usual resistance of the q2DEG at room temperature is much larger than the resistance of the metal, we shall say that 100% of the current in the system is flowing in the metal at room temperature. This room temperature metal resistance will also be assumed to have no dependence with temperature. At this point it is important to note that these assumptions give our analysis a more qualitatively character than a quantitatively one.

But is it safe to use this simple parallel conduction model? Since we are simultaneously sourcing the two metallic layers, other effects regarding the

[7] We believe that the transport properties of the three configuration would be similar, however it is possible that in the $SrTiO_3$ case, oxygen vacancies would form at the interface, and again two contributions would be measured. Metal/SiO_2 would most likely give the most secure metal only measurement.

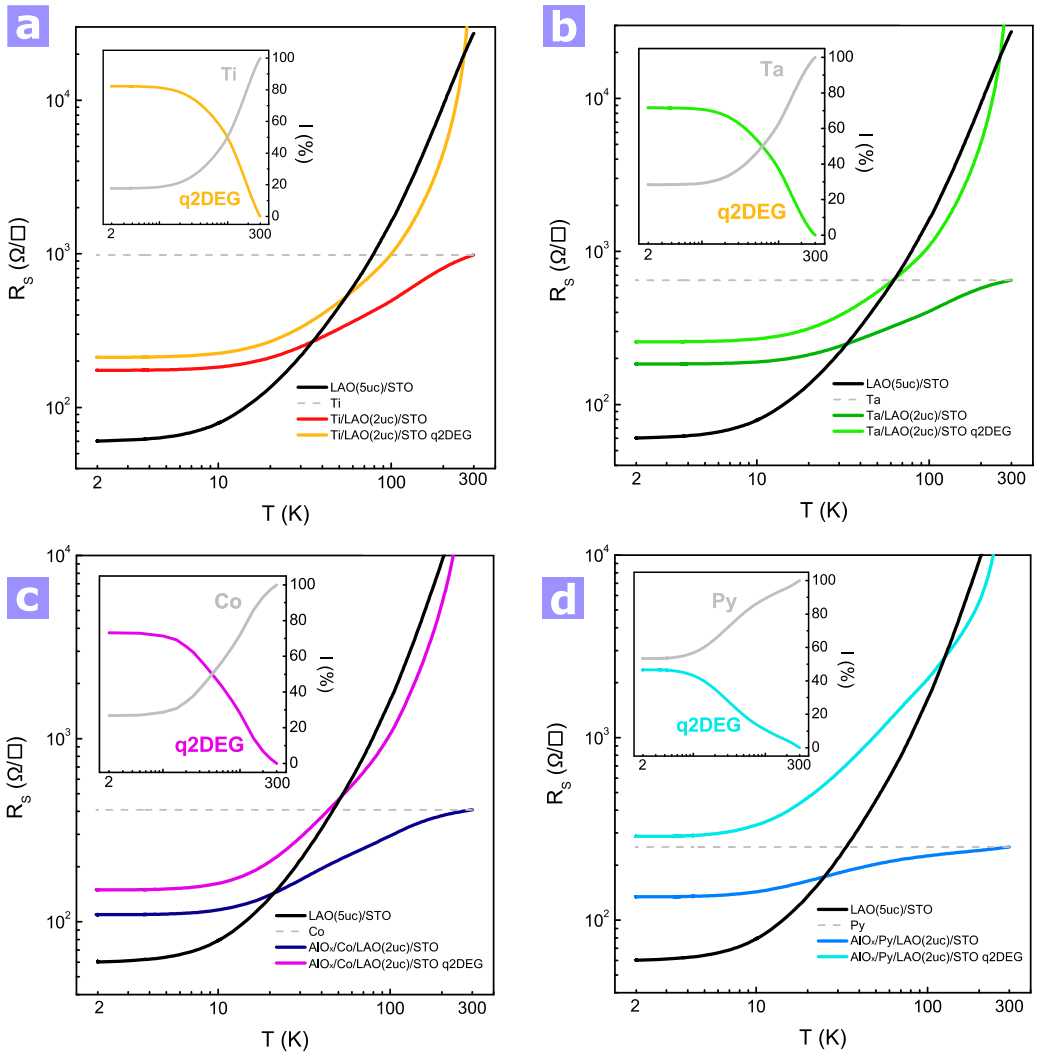

Figure 12 - Sheet resistance as a function of temperature using different metal cappings on $LaAlO_3$ (2uc)/$SrTiO_3$. Measured longitudinal resistance R_{xx}^{meas} (strong colored curve) and R_{xx}^{q2DEG} (light colored curve) extracted with the parallel currents of the metal and q2DEG (inset) for **a)** Ti **b)** Ta **c)** AlOx/Co and **d)** AlOx/Py. The sheet resistance of the previous $LaAlO_3$ (5uc)/$SrTiO_3$ (black curve) is used for comparison. The metallic layer's sheet resistance is assumed to be equal to R_{xx}^{meas} at room temperature and to have no dependence over the temperature sweep.

proximity of both conductive paths, like tunneling of electrons through the extremely thin $LaAlO_3$, do not need to be regarded.

Inspired by Figure 4 [30], we plot in Figure 12 the sheet resistance for four different metal/$LaAlO_3$/$SrTiO_3$ heterostructures, using Ti, Ta, Co and Py as metal cappings and a $LaAlO_3$ thickness of only 2 uc. $LaAlO_3$/$SrTiO_3$ heterostructures (without cappings) with less than 4 uc are known to be insulating, however

we can see that the light colored curve of each plot (q2DEG contribution only) is very similar to the 5 uc $LaAlO_3/SrTiO_3$ sample measured before (black curve). These results suggest that not only the theoretical predictions on the formation of a q2DEG made by Arras *et al*. were correct, but also that the critical thickness suppression observed by Lesne *et al*. in Co capped $LaAlO_3$ (n<4 uc)/$SrTiO_3$ extends to other metals. An additional inset in each plot shows the current distribution within the two metallic paths over temperature, calculated with the resistance relation showed by eq. (13) and taking into account the assumptions made previously. Ti, Ta and Co capped structures show a dominance of the q2DEG current over the metal current at lower temperatures. Interestingly, the q2DEG current in the Py capped structure never goes above the metal current, which hints for the possible importance of a deeper analysis of the electrical characterization of metal (only) samples.

Regarding Hall measurements, the curves were antisymmetrized following the procedure described in Annex 2 – Antisymmetrization and Symmetrization Method in order to remove possible misalignment of contact geometry. For the 5 uc sample analyzed previously (Figure 11), the Hall trace is reasonably linear at low temperatures and shows a total carrier concentration of 3×10^{13} cm^{-2}. However, as depicted in Figure 13 the Hall trace for metal capped structures shows a clear non-linear behavior. Moreover, at 300 K we only see a contribution of the metal, an effect that is very clear especially in Figure 13c, where the Co anomalous Hall effect is observed for magnetic fields below 1.2 T (characteristic of a ferromagnetic metal) and a weak negative slope is present for magnetic fields above 1.2 T. This slope of -23 mΩ/T translates in a carrier density of ~10^{23} cm^{-3}, typical for a (3D) metal.

From [41] we know that when there are multiple types of carriers contributing to conduction, the Hall field must be a compromise between the multiple Hall fields that would be created by each type of carrier independently. The non-linearity observed at low temperatures is therefore attributed to multi band conduction, indicating possible population of d_{xy} and $d_{xz/yz}$ bands. This means that the one band analysis discussed in 3.2.1 and 3.2.2 will be insufficient. To go around this issue, a two-band model has been used by a number of authors

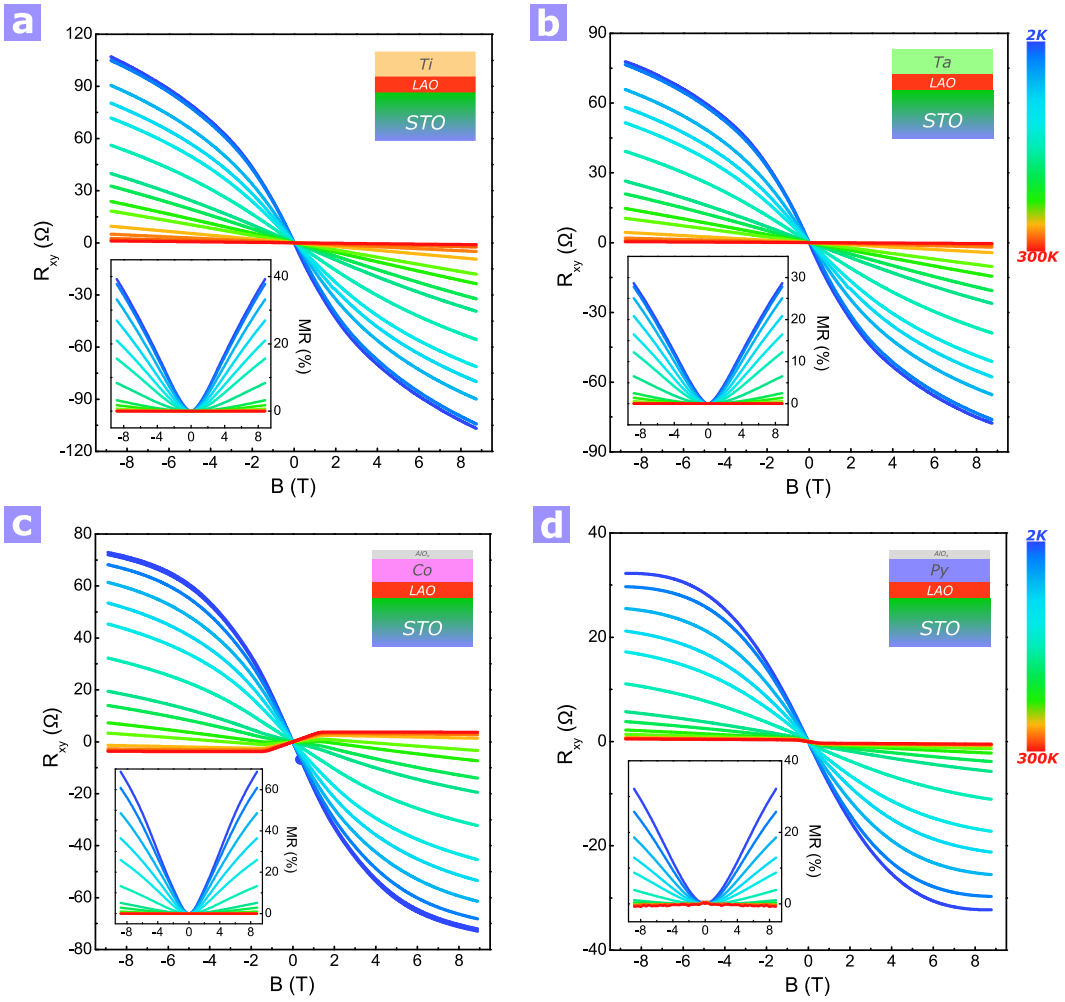

Figure 13 - Hall effect measurements using different metal cappings on $LaAlO_3$ (2uc)/$SrTiO_3$. For all samples, **a)** Ti **b)** Ta **c)** AlO_x/Co and **d)** AlO_x/Py, the room temperature hall effect is dominated bt the metal (red) while at low temperatures a non-linear hall trace appears with different hall coefficients (high field regime) for each sample. Magnetoresistance is also represented in the inset of each figure.

to determine separate carrier concentrations and mobilities. This model takes the form of [42]:

$$R_{xy}(B) = BR_H = B\frac{1}{q}\frac{(n_1{\mu_1}^2 + n_2{\mu_2}^2) + (n_1 + n_2)(\mu_1\mu_2 B)^2}{(n_1\mu_1 + n_2\mu_2)^2 + (n_1 + n_2)^2(\mu_1\mu_2 B)^2} \qquad (14)$$

where (n_1, μ_1) and (n_2, μ_2) are transport coefficients for two different bands. As we see the complexity increases compared to the simple approach of eq. (9) and (11). A number of publications use this model to fully extract carrier concentration and mobilities for two bands contributing to conduction in the system [43–

47]. However, as briefly discussed in [34] supplementary, the model has to be used with caution. Eq. (14) assumes that R_{xy} behaves similarly in both low and high magnetic field regimes, yet, further consideration need to be made.

In the low magnetic field regime (<1 T), the slope of the Hall trace takes the form of:

$$R_H^0 = -\frac{(n_1{\mu_1}^2 + n_2{\mu_2}^2)}{q(n_1\mu_1 + n_2\mu_2)^2} \tag{15}$$

This slope, contrary to the simple inverse relation with carrier concentration (eq. (9)), represents a mobility-dependent mean carrier concentration in the system. Joshua *et al*. [34] noted that while extracting transport parameters using the two band model and gate dependence, the total carrier concentration decreases with increasing gate voltage (increasing doping), a clear non-physical behavior. Rewriting the model using three bands instead of two, more realistic Fermi surfaces or including the effect of ASO could maybe reduce deviations from real values, but the complexity of calculation would increase exponentially.

For a large magnetic field regime (≫1 T), the slope can be written as:

$$R_H^\infty = -\frac{1}{q(n_1 + n_2)} \tag{16}$$

In this case the total carrier concentration in the system $n_S = (n_1 + n_2)$ can be extracted. Although the above equation was deduced at the limit of large magnetic field regime, the +-9T used in our experiments should suffice to extract fairly acceptable parameters. In the four plots displayed in Figure 13 the slope decreases with increasing magnetic field. Arras *et al*. predicted higher carrier concentrations for metal capped $LaAlO_3/SrTiO_3$ structures. This might be due to doping from the metal, since the electrostatic boundary conditions at the $LaAlO_3$ surface are different from bare $LaAlO_3/SrTiO_3$ samples. Accordingly, from the experimental data, n_S equals 1.05, 1.80, 3.43 and 165 ($\times 10^{14}$) cm^{-2} for Ti, Ta, Co and Py capped structures, respectively. The carrier concentration achieved for the Py capped sample is indeed much larger than expected for the q2DEG alone, which might indicate that a contribution of the metal might be present. Additionally we estimated the mobility of the q2DEG. In this case we assume for the sake

of simplicity that the contribution of the very thin metallic films for the Hall response is negligible, since μ_M should be less than 1 $cm^2/(V.s)$. Mobilities of 280, 134, 121 and 1.35 $cm^2/(V.s)$ for Ti, Ta, Co and Py capped structures, respectively, were obtained. These values are lower than the $4000\ cm^2/(V.s)$ of the 5 uc $LaAlO_3/SrTiO_3$ sample analyzed. However, these are nothing but a balanced mobility of both types of carriers (maybe three if the metal is considered). It is possible that carriers in one of the bands are in fact much slower while the other type reaches mobility values near the ones achieved for $LaAlO_3/SrTiO_3$ samples. MR values (inset of Figure 13) calculated for each sample show yet again that at room temperature only the metal is conducting, hence the flat MR observed for all samples. At low temperatures MR ranges between 30% and 60%, which reinforces our belief regarding the presence of a q2DEG and its dominance in the parallel conduction model.

Although all the metals used above seem to induce a q2DEG in the system, another scenario is observed for a second set of metal cappings. Figure 14 shows the Hall trace for Au, Pt and Pd capped $LaAlO_3$ (2uc)/$SrTiO_3$. Both longitudinal resistance values and slopes achieved are shockingly different from the previous four samples. The Hall trace is also perfectly linear for the range of magnetic field used, with R_H of 20, 17 and 5 mΩ/T for Pd, Au and Pt capped structures respectively. These values lead to 3D-like carrier concentration of $\sim 10^{23}\ cm^{-3}$ supporting the fact that we are only measuring the Hall trace of the metallic layer, and therefore no q2DEG is present in the system. The extremely low MR further strengths this conclusion.

In addition, a parallel can be made with the analysis of Caviglia *et al*. [35] seen in fig. 10e. The magnetoconductance of the four samples of the first series is shown in Figure 15. σ_{2D}^0 was calculated with Drude's formula from eq. (10) adapted for 2D system. A small bar on the top indicates the magnetotransport regime according to σ_{2D}^0 (adapted from [39]). It seems that for the calculated values, our samples are on what Fête *et al*. calls the "Anomalous Metal regime". In this regime the carrier concentration is larger than in the WL and WAL, which is exactly what we saw previously. We can also say that these curves are analogous to a highly electrostatic doped $LaAlO_3$ (n>4 uc)/$SrTiO_3$ where high positive gate voltage is applied (bottom curves of the plot in fig. 10b).

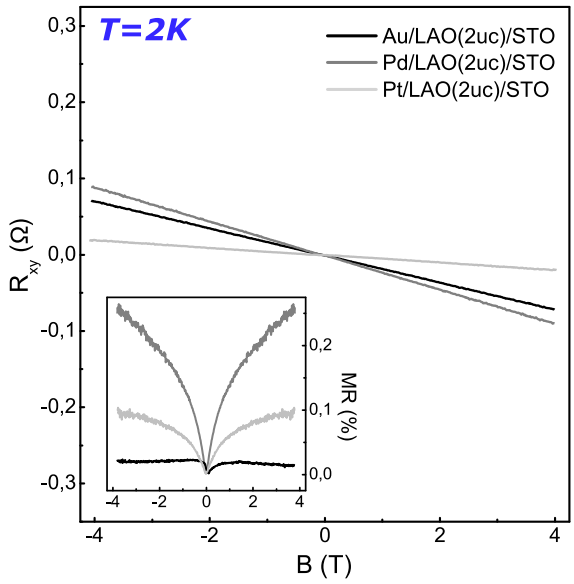

Figure 14 - Hall effect measurements using Au, Pd and Pt as metal cappings on $LaAlO_3$ (2uc)/$SrTiO_3$ and corresponding magnetoresistance (inset). The linear Hall effect and the low values of magnetoresistance at high fields show that there is no formation of a q2DEG.

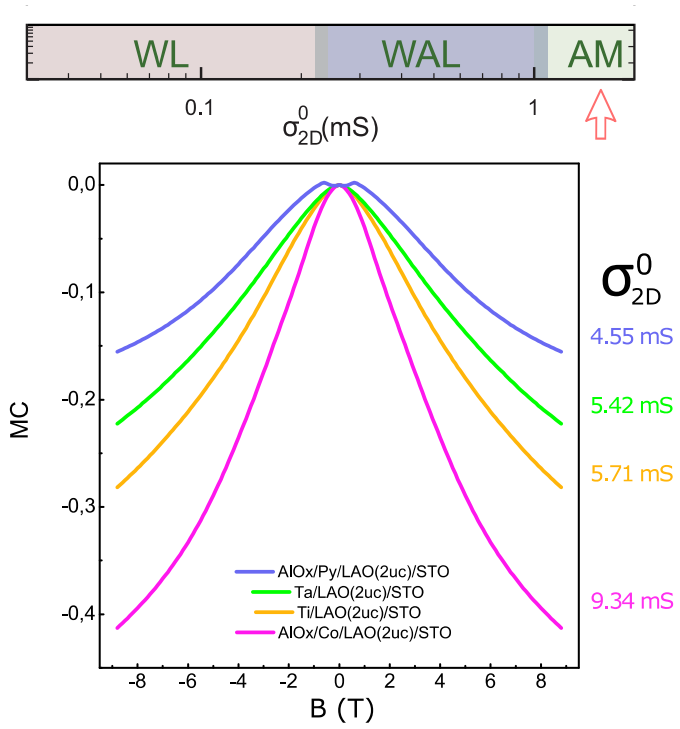

Figure 15 - Magnetoconductance calculated for metal/$LaAlO_3$ (2uc)/$SrTiO_3$ (metal: Py, Ta, Ti, Co). The bar at the top situates the sample's magnetotransport regime according to the sheet conductance at zero field σ_{2D}^0 (modified from [39]). The high σ_{2D}^0 obtained indicate that the metal capped $LaAlO_3/SrTiO_3$ samples measured are in the Anomalous Metal regime, characterized by large carrier concentrations.

Tuning our samples with gate voltage could enable the transition into the WAL regime, where, as we saw in fig. 10b, the SOI strength is the highest. These experiments will be mentioned in the conclusion as future work, since it will be essential to maximize the SOI strength for further spin-to-charge conversion at the $LaAlO_3/SrTiO_3$ interfacial q2DEG using the inverse Rashba-Edelstein effect [48].

Even if the extraction of exact transport parameters in metal capped $LaAlO_3/SrTiO_3$ structures is without a doubt a hard task, one thing can be concluded with a high degree of certainty. The properties of the q2DEG strongly depend on the choice of metal used as capping layer. In the next chapter we shall propose two scenarios that give further insight on this dependence and might even explain why some metals do not induce a q2DEG at all.

3.3. q2DEG Formation

3.3.1. Critical Work Function Scenario

Undoubtedly, the metal has an effect on the formation and behavior of the q2DEG at the $LaAlO_3/SrTiO_3$ interface. From the transport data analyzed previously, different metals lead to different carrier concentrations and mobilities. This is indeed a very powerful way to tune the functionality of the gas, but makes us wonder how the gas is formed in the first place (for a $LaAlO_3$ thickness bellow 4 uc). In Chapter 1 we discussed two general approaches: one regarding a pure intrinsic electrostatic model and another the formation of defects such as oxygen vacancies. In the first one, the $LaAlO_3$ band is bended due to the internal electric field, thus reaching the conduction band of $SrTiO_3$. Electrons will travel to the interface and the internal field is almost completely cancelled. In our case, 2 uc (without capping) are not sufficient to bend the $LaAlO_3$ bands completely. So what changes by adding a metal layer and in what way is the band structure influenced?

Let us first look at an ideal metal-semiconductor junction. When a metal and a semiconductor are brought together the Fermi level of both materials should align. The matching Fermi levels leads to charge transfer from one side to another (also theoretically observed for metal-oxide junctions [49]). Due to the

high density of conduction electrons on the metal side, the charge imbalance is screened within a few Ångstroms, while this effect is much less effective in the semiconductor. Due to the charge transfer dipoles formed at the interface, band bending will occur with a height associated with the work function ϕ_M of the metal and the electron affinity χ_{SC} of the semiconductor. The maximum band bending defines the Schottky barrier height ϕ_{SB} [50]. In reality, the formation of such junctions also induces localized states, such as metal-induced gap states (MIGS), which will depend on interface orientation, growth conditions and detailed atomic structures. These states will dominate the band alignment over the previously described mechanism [51]. However, since we are dealing with a perovskite oxides, these localized in-gap interface states are less likely to appear. It was found that there is almost no Fermi level pinning at metal/$LaAlO_3$ interface and the band alignment is largely determined by interface chemistry [52].

In order to give a glimpse of what the band structure of the heterostructures might look like, we display in Figure 16a the band diagram when the $LaAlO_3/SrTiO_3$ junction is achieved (values taken from [53] supplementary). First of all, we can see the confinement potential on the $SrTiO_3$ side, where electrons will stay to form the 2DEG. The potential depth is believed to appear due to the mismatch of electron affinities between both materials and was attributed a value of around $PWD = 0{,}3$ eV according to hard x-ray photoelectron spectroscopy and density functional theory calculations [23,54,55]. On the $LaAlO_3$ we see that band bending is present. It is known that due to the polar discontinuity at the interface a built-in electric field of ~6 V/Å is observed [17]. Yet, it is argued that due to polar distortions in the $LaAlO_3$ a significant reduction of the internal field occurs, leading to a total value of ~0.24 V/Å. This mechanism delays the crossover of the valence band with $SrTiO_3$ conduction band. Without it, the system would be metallic for any coverage of $LaAlO_3$ [56]. The potential shift $\Delta\phi$ that the $LaAlO_3$ band experiences will therefore depend on the built-in field E_{LAO} above mentioned and additionally on the film thickness t_{LAO}:

$$\Delta\phi = eE_{LAO}t_{LAO} \tag{17}$$

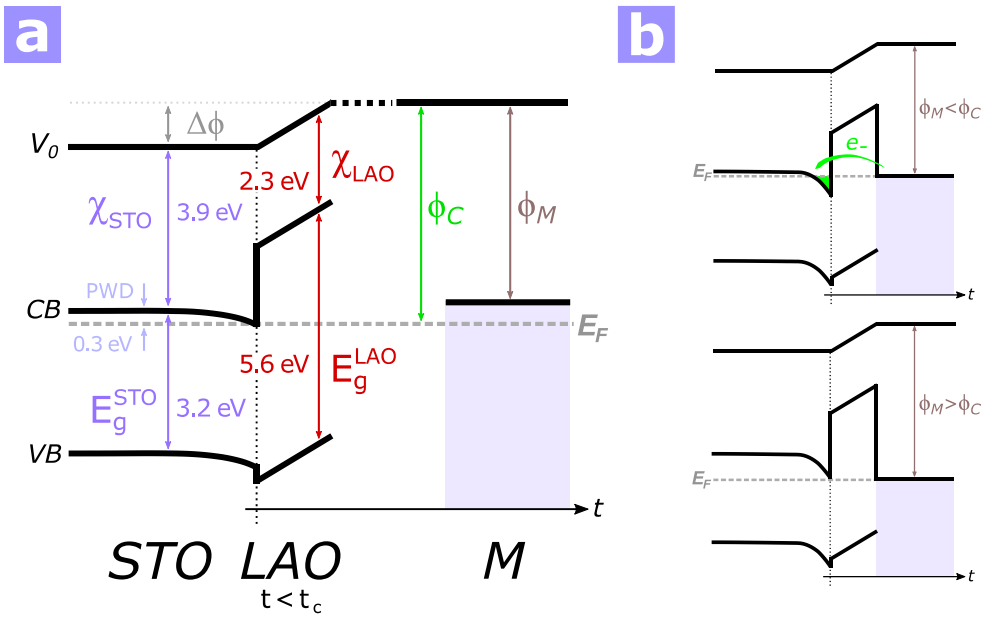

Figure 16 - Schematic energy band diagram of metal/$LaAlO_3$ (n)/$SrTiO_3$ with n<t_c=4uc. a) Band diagram prior to contact between the metal and $LaAlO_3$. X_{STO} and X_{LAO} are the insulator's electron affinity, E_g^{STO} and E_g^{LAO} the band gap, E_F and V_0 the Fermi level and vacuum level, respectively. PWD is the potential well depth, ϕ_M the work function of the metal and ϕ_C the critical work function given by eq. (18). **b)** When in contact, if ϕ_M is smaller than ϕ_C charge transfer occurs towards the $SrTiO_3$ conduction band. If ϕ_M is larger than ϕ_C the Fermi level will lie inside the $SrTiO_3$ bandgap and no charge transfer occurs. The interface remains therefore insulating.

Already we notice that the calculation of these energies is extremely sensitive and will inevitably accumulate deviations from all the above mentioned phenomena.

In metal/$LaAlO_3$/$SrTiO_3$ heterostructures the electrostatic boundary conditions change and complexity increases. Due to surface charges introduced by the metal, the internal field is expected to decrease further, with complete attenuation for some metals [29]. The chemical bonding of the metallic species (with the oxygen and between them) also results in different structural relaxations within the system, and consequently in a variation of the lattice polarization of $LaAlO_3$. It was also found that the internal field decreases with increasing $LaAlO_3$ thickness, which rules out the possibility of a Zener breakdown, the central piece of the whole polar catastrophe model [57].

The estimation of $\Delta\phi$ for the metal capped heterostructures is therefore a difficult task. Nevertheless, we shall analyze the possibility of a critical metal work function ϕ_C based on the transport properties obtained for metal/$LaAlO_3$/$SrTiO_3$ samples with different metals.

First of all, the electrons available for conduction most likely come from the metal. They will travel across the $LaAlO_3$ thin layer and reach the Ti 3d states in the $SrTiO_3$ by, what is believed to be, multistep tunneling. The occurrence of this phenomenon is supported by the conductance dependence of Co/$LaAlO_3$/ $SrTiO_3$ junctions with temperature [58]. Note that the $LaAlO_3$ barrier prevents the contact between the metal electrode and the $SrTiO_3$, which to some extent simplifies our analysis by removing possible direct interaction between charges on both sides. We then can deduce a simple way to calculate ϕ_C, having in consideration the $LaAlO_3$ potential shift $\Delta\phi$, the potential well depth PWD in the $SrTiO_3$ and the bulk electron affinity of $SrTiO_3$ χ_{STO}:

$$\phi_C \approx \Delta\phi + \chi_{STO} + PWD \tag{18}$$

Figure 16a can be used to visualize the expression above. ϕ_C represents the maximum work function that a metal might have so that electrons are allowed to travel into the $SrTiO_3$. But can we fully trust this value? Unfortunately the answer is no. As we saw previously the biggest concern lies on $\Delta\phi$ as it depends on other variables that are also difficult to attain with sufficient accuracy. However, some estimations can be made. Assuming no shift is present in the $LaAlO_3$, $\Delta\phi = 0$ eV and we obtain a minimum value of $\phi_C = 4.2$ eV. The maximum internal field for metal capped structures is theoretically known to monotonically decrease with increasing thickness of $LaAlO_3$ [57]. This means that the highest band bending is achieved for 1 uc samples which excludes a Zener breakdown mechanism. This approach goes therefore against the polar catastrophe model, where a Zener breakdown is expected at 4 uc. Since the precise value of the internal field is also dependent on surface and interfacial charge densities, achieving an exact value is problematic. However, from [57] we can estimate a maximum value of $\Delta\phi = 0.3$ eV. Since the maximum internal electric field was calculated for Pt/$LaAlO_3$/$SrTiO_3$ heterostructures, it is assumed that it may vary a few meV for

different choices of metal [29]. Ultimately, this translates into a ϕ_C that ranges approximately between 4.2 and 4.5 eV.

Let us then draw some conclusion regarding this simple electrostatic model and our transport data. For a metal capping with $\phi_M > \phi_C$ we expect the Fermi level to lie within the bandgap of $SrTiO_3$, preventing any charge transfer into the well and consequently leaving the interface insulating (as depicted in Figure 16b). Yet, for a capping with $\phi_M < \phi_C$, the Fermi level lies above the $SrTiO_3$ conduction band. Charge is then able to travel into Ti 3d states at the interface, resulting in the formation of a q2DEG below the established critical thickness of 4 uc of $LaAlO_3$. Metals with $\phi_M > 4.5$ eV should not therefore allow the formation of a q2DEG. However, as seen from transport experiments, a conductive interface is observed for Co and Py cappings, which goes against the critical work function scenario. Two remarks must be made at this point. The first one is that the metal work functions considered are variable (Table 1), depending on factors such as cleanliness of the surface and orientation of the crystal. A deviation over hundreds of meV is therefore expected. Finding the exact values for Py is even a more difficult task. It has been shown for other binary alloys that calculations go beyond a simple linear interpolations between the work function of both bulk materials [59]. The second remark targets the critical work function values assumed. Experimentally, ϕ_C should be around 5.1 eV. The discrepancy between theoretical and experimental values of 1 eV might be explained by the amount of consideration made in the simple electrostatic model above. The internal field of $LaAlO_3$ plays a crucial role on this analysis and at the same time is our most "fragile" parameter. Other phenomena such as electrochemical reactions may play an important role as well. In the end, this scenario neither proves nor disproves the existence of a critical work function. At best, it can be seen, among many others, as an additional scenario for the formation of the q2DEG. Supplementary insights are mentioned in the concluding remarks of this dissertation, regarding some experiments that may clarify the uncertainties of this model.

Table 1 – Work functions of the metals used as capping layers [60]**.**

Metal	Ta	Ti	Co	Py	Au	Pd	Pt
ϕ_M(eV)	4.25	4.33	5.0	5.20	5.1	5.12	5.65

3.3.2. Metal-Induced Oxygen Vacancies Scenario

In the framework of the polarity-induced defect mechanism proposed by Yu and Zunger [24], briefly introduced in chapter 1, the increase of $LaAlO_3$ thickness leads to an increasing of the internal field that will favor thermodynamically the formation of defects at 4 uc. At this thickness, oxygen vacancies favorably formed at the surface of $LaAlO_3$ will provide electrons that travel into Ti 3d bands at the interface. However the deposition a metal on top of the structure inevitably changes the boundary conditions of this interpretation.

The idea is that in $LaAlO_3/SrTiO_3$ structures the formation of oxygen vacancies is dependent on the thickness of $LaAlO_3$ and consequently on the internal field present. In the case of metal/$LaAlO_3/SrTiO_3$ structures, this dependence disappears. When a metal is in contact with a rich oxygen structure, such as $LaAlO_3$, it will tend to oxidize. The oxygen is then expected to be "pulled" into the metallic side of the interface, leaving vacancies behind. This process may in fact happen for any thickness of $LaAlO_3$, and therefore oxygen vacancies at the surface of $LaAlO_3$ will be present for thicknesses 1, 2 and 3 uc as well. This perspective might explain why our thin $LaAlO_3$ samples show a formation of a q2DEG. But what about the case of the metals (Au, Pt, Pd) that do not show any sign of a conducive interface? Since this scenario relies on the oxidization of the metal it may be interesting to look at the enthalpy of formation (ΔH_0). This parameter can be interpreted as a sum of many separate processes, but for this case we will simply interpret it as the tendency for a metal to form an oxidized phase. We show, in Table 2, ΔH_0 values for the different metals used in our experimental analysis[8]. A higher (negative) ΔH_0 translates in higher propensity for the metal to oxidize, while metals with low ΔH_0 are very difficult to oxidize. It can be seen that nobel metals are extremely resistant to direct chemical combination with oxygen, and therefore show the lowest ΔH_0 of the whole set. Experimentally our transport results go along with this scenario, as we evidenced that using nobel metals as a capping layer does not lead to the formation of a q2DEG. However,

[8] Just like in the above section, these values are variable depending on the specific conditions of the metal in question. In this sense, they are presented here to support a merely qualitatively evaluation of the proposed scenario.

could there possibly be a critical enthalpy of formation for which the metal induces enough oxygen vacancies to unlock the interfacial conductivity? Unfortunately, so far this scenario has not yet been addressed or discussed in the bibliography. A thorough theoretical study on the enthalpy of formation of metal oxide phases and other defects would be necessary to draw stronger conclusions.

Table 2 – Enthalpies of formation of the metals used as capping layers [61–63]**.**

Metal	Ta	Ti	Co	Py	Au	Pd	Pt
ΔH_0(kcal)	-180	-213	-100	-105	-3	-43	-24

3.3.3. Influence of ϕ_M and ΔH_0 on Transport Properties

Over the last two sections we discussed the possibility of a critical work function and a critical enthalpy of formation regarding the appearance of a q2DEG in $LaAlO_3/SrTiO_3$ structures with less than 4 uc. Yet, is it possible to find a trend between the nature of the metal that enables the formation of a q2DEG and its transport properties?

For this purpose, we plotted the relation between work functions (Figure 17a) and enthalpies of formation (Figure 17b) for Ti, Ta, Co, Py, Au, Pt and Pd with the total carrier concentrations calculated from Hall measurements of Figure 14 and Figure 15.

As stated before, metals with higher work function do not form a q2DEG. A trend is however not observed for the metals that form a q2DEG. We would expect that the Ta capped sample would show a lower carrier concentration than the Ti capped sample, since its work function is lower. A lower work function does not seem to induce more carriers into the q2DEG. In fact it seems that the trend is reversed, in the sense that with increasing difference between the Fermi level of the metal and the conduction band of $SrTiO_3$, the metal seems to induced less carriers. In a pure electrostatic model, one would expect a minimum carrier concentration in the q2DEG for a metal with the Fermi level at the same energy as the conduction band of $SrTiO_3$.

Additionally, just like mentioned in the transport analysis, the Py leads to extremely high total carrier concentrations (not displayed). Further considerations regarding the metal contribution should be made.

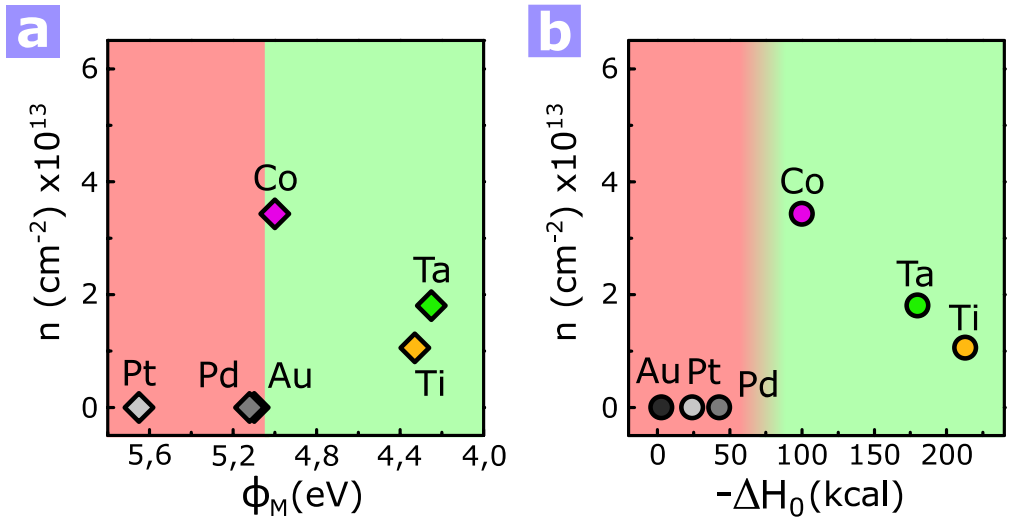

Figure 17 - Influence of the metal on the carrier concentration calculated for each sample. **a)** Metals with lower work function allow the formation of a q2DEG. An experimental critical work function can be estimated (green/red boundary). **b)** The tendency of the metal to oxidize given by the enthalpy of formation ΔH_0 also influences the formation or not of a q2DEG. Metals with larger (negative) ΔH_0 form more oxygen vacancies at the $LaAlO_3$ surface but lead to lower carrier concentrations in the system. Metals like Au, Pt and Pd are not as likely to oxidize. In this case no oxygen vacancies are formed and the system stays insulating. A critical enthalpy of formation is in this case harder to extract (green/red gradient).

For the second case (right side) a critical enthalpy of formation scenario might be difficult to prove. Additional consideration can be made inside the set of metals that do form a q2DEG. Should a metal with higher ΔH_0 form more oxygen vacancies at the $LaAlO_3$ surface? Do more oxygen vacancies mean higher availability of electrons that can travel into the Ti 3d states? A clear trend is in this case seen, but again reversed from what would be expected. From Figure 17b we see that metals with higher enthalpy of formation leads to a q2DEG with less carriers, which is counter intuitive, since a higher formation of vacancies should release more electrons in the system. Charge accumulation and screening effects should be taking into consideration for future analysis. Nevertheless, ΔH_0 close to zero indicate almost no formation of an oxide phase and therefore does not allow the formation of a q2DEG.

Even if this analysis might gather simple features of both mechanism, it cannot be considered as a definitive qualitative evaluation. Besides the eventual

deviation associated with work functions and enthalpies of formation considered, the carrier concentrations calculated are too sample-to-sample dependent. The Py case further increases our doubts and may even put in question the reliability of the two-band model. What this means is that for a proper analysis, gate dependence should be used in order to place every sample in the same "state", where for example all carrier concentrations match. These experiments will be mentioned in the conclusion as future work.

4

Conclusion and Perspectives

In this dissertation, we have analyzed the magnetotransport properties of metal/$LaAlO_3$/$SrTiO_3$ heterostructures bellow the known critical thickness of 4 uc of $LaAlO_3$. We started by giving a brief introduction on the metallic behavior of the $LaAlO_3$/$SrTiO_3$ interface. The first issue discussed regards the formation of a q2DEG at the interface and its origin. A number of scenarios have been proposed to justify the underlying physics of this system, however none of them is fully satisfactory on its own. Although a mix of the scenarios is most likely the best way to look at the q2DEG formation, a quantitatively contribution of each one is hardly achievable. The second focuses on the importance of reducing the $LaAlO_3$ thickness for efficient spin detection in devices.

We start by growing and analyzing thick $LaAlO_3$ (5uc) /$SrTiO_3$. A great number of publication have been submitted since the discovery made by Ohtomo and Hwang in 2004 [1], yet, the need of a good platform for growing proper metal/$LaAlO_3$/$SrTiO_3$ heterostructures is of the upmost importance. A combination of PLD and RHEED was used to epitaxially grow the $LaAlO_3$ layer. The properties of the grown samples were very similar to the ones seen in the bibliography, with carrier concentrations of $n_S = 3 \times 10^{13}$ cm^{-2} and mobilities of $\mu = 4000$ cm^2/(V. s).

By establishing a good growing procedure, we moved to the deposition of a metal by magnetron sputtering on top of thin $LaAlO_3$ (<4uc)/$SrTiO_3$ structures. The predictions made by Arras *et al*. [29] and the q2DEG formation in

Co/$LaAlO_3$/$SrTiO_3$ samples from our group [30] incentivized the usage of different metal cappings as a way to tune the properties of the q2DEG and at the same time achieve a more profound study on the system. We have grown and analyzed metal/$LaAlO_3$ (2uc)/$SrTiO_3$ samples using Ti, Ta, Co, Py, Au, Pt and Pd as metallic capping layers.

We used a simple parallel conduction model that takes into account the contribution of the current flowing in the metal and the q2DEG. The sheet resistance analysis of these samples demonstrates that a behavior similar to the uncapped thick $LaAlO_3$ (>4uc)/$SrTiO_3$ is achieved, which proves the formation of a q2DEG for low thickness of $LaAlO_3$. The Hall measurements reveal higher carrier concentrations (at high fields and low temperatures), as predicted by Arras *et al*. theoretically. However, the specific case of Py capped structures is quite intriguing. The slope of the Hall trace between 9 and 8 T is almost flat, resulting in calculated carrier concentrations in the order of 10^{15} cm^{-2}, a value that seems unphysical for the q2DEG alone. However, the carrier concentration for high fields, as demonstrated in eq. (16), is independent of both carrier mobilities. If the effect of the metal is not ignored, we can assume that n_1 and μ_1 describe all the possible bands of the q2DEG, and that n_2 and μ_2 are related to the metal. In this case, it should be expected that for high enough fields (maybe even $B_{critical}$) the slope of all metal capped $LaAlO_3$/$SrTiO_3$ structures would go almost flat. In this regime n_2 (metal) would dominate over the smaller n_1 present in the q2DEG. An analysis at higher magnetic fields (>9 T) should clarify these hypothesis. A deeper analysis of the two band model (eq. (14)) accompanied with simulations for different values of n_1 and μ_1 for different magnetic fields applied should also further improve the understanding of the conduction in the system.

Using gate voltage will be fundamental to enable a correct comparison between different capped samples. Although some qualitatively conclusion are drawn in this dissertation, in order to have a proper quantitatively analysis, gate voltage should be used to tune the carrier concentration of each sample. An additional analysis to the chemical state of Ti 3d states using X-ray photoelectron spectroscopy (XPS) at the interface would also be of great interest. Our current PLD system would indeed enable the growth of 1 uc at a time and, in between

each uc, use XPS to observe any energy shifts of the atoms core levels at the metal/$LaAlO_3$ and $LaAlO_3/SrTiO_3$ interface.

Regarding the two discussed scenarios on the formation of the q2DEG, additional methods would be required to analyze the actual work function and enthalpy of formation for the thin metal layers used. Additional metals such as Cr, Mn, Nb and Cu could be used in order to draw a wider picture on the effect of the properties of the metal on the q2DEG. As we saw, the band bending $\Delta\phi$ is the main obstacle regarding the critical work function scenario. The use of synchrotron-based X-ray diffraction could be useful to elucidate on the presence (or absence) of a built-in electrostatic potential in metal capped structures. Additionally, the analysis of Figure 17 opens a new perspective on how to look at the q2DEG formation. However, the two band model issues mentioned above highly influence these results. For carrier concentrations calculated at a different range of magnetic fields, the Hall coefficients would be different. This analysis would suffer a huge improvement if the isolation of the carrier concentrations and mobilities of the q2DEG bands is achieved. Again, applying gate voltage will help to develop a broader view.

All these suggestions will be tackled in the future in the hopes of building a solid base for future spin injection/detection in these types of structures. By resolving the high resistance imposed by the $LaAlO_3$ layer, conversion of spin-to-charge current using the inverse Rashba-Edelstein effect will be tested similarly to the experiments conducted by Rojas-Sanchez *et al.* [48] in Ag/Bi interfaces. Using different metals and tuning the structures with gate voltage will allow us to move between WL and WAL regimes in order to find at which conditions the spin-orbit interaction strength is maxed (Figure 10d).

5

References

1. Ohtomo, A. & Hwang, H. Y. 2004 A high-mobility electron gas at the LaAlO3/SrTiO3 heterointerface. *Nature* **427**, 423. (doi:10.1038/nature02308)

2. Nishimura, J. et al. 2004 Controlled carrier generation at a polarity-discontinued perovskite heterointerface. *Jpn. J. Appl. Phys.* **43**, 1032. (doi:10.1143/JJAP.43.L1032)

3. Nakagawa, N. et al. 2006 Why Some Interfaces Cannot be Sharp. *Nat. Mater.* **5**, 204. (doi:10.1038/nmat1569)

4. Reyren, N. et al. 2007 Superconducting interfaces between insulating oxides. *Science (80-.).* **317**, 1196. (doi:10.1126/science.1146006)

5. Brinkman, A. et al. 2007 Magnetic effects at the interface between non-magnetic oxides. *Nat. Mater.* **6**, 493. (doi:10.1038/nmat1931)

6. Basletic, M. et al. 2008 Mapping the spatial distribution of charge carriers in LaAlO3/SrTiO3 heterostructures. *Nat. Mater.* **7**, 621. (doi:10.1038/nmat2223)

7. Copie, O. et al. 2009 Towards two-dimensional metallic behavior at LaAlO3/SrTiO3 interfaces. *Phys. Rev. Lett.* **102**, 216804. (doi:10.1103/PhysRevLett.102.216804)

8. Caviglia, A. D. et al. 2010 Two-dimensional quantum oscillations of the conductance at LaAlO3/SrTiO3 interfaces. *Phys. Rev. Lett.* **105**, 236802. (doi:10.1103/PhysRevLett.105.236802)

9. Thiel, S. et al. 2006 Tunable quasi-two-dimensional electron gases in oxide heterostructures. *Science (80-.).* **313**, 1942. (doi:10.1126/science.1131091)

10. Popović, Z. S. et al. 2008 Origin of the two-dimensional electron gas carrier density at the LaAlO3 on SrTiO3 interface. *Phys. Rev. Lett.* **101**, 256801. (doi:10.1103/PhysRevLett.101.256801)

11. Pentcheva, R. & Pickett, W. E. 2009 Avoiding the polarization catastrophe in LaAlO3 overlayers on SrTiO3(001) through polar distortion. *Phys. Rev. Lett.* **102**, 107602. (doi:10.1103/PhysRevLett.102.107602)

12. Takizawa, M. et al. 2011 Electronic charges and electric potential at LaAlO3/SrTiO3 interfaces studied by core-level photoemission spectroscopy. *Phys. Rev. B* **84**, 245124. (doi:10.1103/PhysRevB.84.245124)

13. Segal, Y. et al. 2009 X-ray photoemission studies of the metal-insulator transition in LaAlO3/SrTiO3 structures grown by molecular beam epitaxy. *Phys. Rev. B* **80**, 241107R. (doi:10.1103/PhysRevB.80.241107)

14. Willmott, P. R. et al. 2007 Structural basis for the conducting interface between LaAlO3 and SrTiO3. *Phys. Rev. Lett.* **99**, 155502. (doi:10.1103/PhysRevLett.99.155502)

15. W., G. et al. 1991 Oxygen-Deficient SrTiO3-x, x=0.28, 0.17, and 0.08. Crystal Growth, Crystal Structure, Magnetic, and Transport Properties. *J. Solid State Chem.* **90**, 320. (doi:10.1002/chin.200613223)

16. Spinelli, a. et al. 2010 Electronic transport in doped SrTiO_{3} : Conduction mechanisms and potential applications. *Phys. Rev. B* **81**, 155110. (doi:10.1103/PhysRevB.81.155110)

17. Cancellieri, C. et al. 2011 Electrostriction at the LaAlO3/SrTiO3 interface. *Phys. Rev. Lett.* **107**, 056102. (doi:10.1103/PhysRevLett.107.056102)

18. Herranz, G. et al. 2007 High mobility in LaAlO3/SrTiO3 heterostructures: Origin, dimensionality, and perspectives. *Phys. Rev. Lett.* **98**, 216803. (doi:10.1103/PhysRevLett.98.216803)

19. Siemons, W. et al. 2007 Origin of charge density at LaAlO3 on SrTiO3 heterointerfaces: Possibility of intrinsic doping. *Phys. Rev. Lett.* **98**, 196802. (doi:10.1103/PhysRevLett.98.196802)

20. Kalabukhov, A. et al. 2007 Effect of oxygen vacancies in the SrTiO_{3} substrate on the electrical properties of the LaAlO_{3}/SrTiO_{3} interface. *Phys. Rev. B* **75**, 121404. (doi:10.1103/PhysRevB.75.121404)

21. Bristowe, N. C. et al. 2011 Surface defects and conduction in polar oxide heterostructures. *Phys. Rev. B* **83**, 205405. (doi:10.1103/PhysRevB.83.205405)

22. Li, Y. et al. 2011 Formation of oxygen vacancies and charge carriers induced in the n-type interface of a LaAlO 3 overlayer on SrTiO 3(001). *Phys. Rev. B* **84**, 245307. (doi:10.1103/PhysRevB.84.245307)

23. Berner, G. et al. 2013 Direct k-space mapping of the electronic structure in an oxide-oxide interface. *Phys. Rev. Lett.* **110**, 247601. (doi:10.1103/PhysRevLett.110.247601)

24. Yu, L. & Zunger, A. 2014 A unified mechanism for conductivity and magnetism at interfaces of insulating nonmagnetic oxides. *Nat. Commun.* **5**, 5118. (doi:10.1038/ncomms6118)

25. Bibes, M. et al. 2012 Towards electrical spin injection into LaAlO3-SrTiO3. *Philos. Trans. R. Soc. A* **370**, 4958. (doi:10.1098/rsta.2012.0201)

26. Schmidt, G. et al. 2000 Basic obstacle for electrical spin-injection from a ferromagnetic metal into a diffusive semiconductor. *Phys. Rev. B* **62**, R4790. (doi:10.1103/PhysRevB.62.R4790)

27. Rashba, E. I. 2000 Theory of electrical spin injection: Tunnel contacts as a solution of the conductivity mismatch problem. *Phys. Rev. B* **62**, 267. (doi:10.1103/PhysRevB.62.R16267)

28. Fert, A. & Jaffrès, H. 2001 Conditions for efficient spin injection from a ferromagnetic metal into a semiconductor. *Phys. Rev. B* **64**, 184420. (doi:10.1103/PhysRevB.64.184420)

29. Arras, R. et al. 2012 Tuning the two-dimensional electron gas at the LaAlO 3/SrTiO 3(001) interface by metallic contacts. *Phys. Rev. B* **85**, 125404. (doi:10.1103/PhysRevB.85.125404)

30. Lesne, E. et al. 2014 Suppression of the critical thickness threshold for conductivity at the LaAlO3/SrTiO3 interface. *Nat. Commun.* **5**, 4291. (doi:10.1038/ncomms5291)

31. Kawasaki, M. et al. 1994 Atomic Control of the SrTiO3 Crystal Surface. *Science (80-.).* **266**, 1540. (doi:10.1126/science.266.5190.1540)

32. Van der Pauw, L. J. 1958 A method of measuring the resistivity and Hall coefficent on lamellae of arbitrary shape. *Philips Tech. Rev.* **20**, 220.

33. Salluzzo, M. et al. 2009 Orbital reconstruction and the two-dimensional electron gas at the LaAlO3/SrTiO3 interface. *Phys. Rev. Lett.* **102**, 166804. (doi:10.1103/PhysRevLett.102.166804)

34. Joshua, A. et al. 2012 A universal critical density underlying the physics of electrons at the LaAlO3/SrTiO3 interface. *Nat. Commun.* **3**, 1129. (doi:10.1038/ncomms2116)

35. Caviglia, A. D. et al. 2010 Tunable Rashba Spin-Orbit Interaction at Oxide Interfaces. *Phys. Rev. Lett.* **104**, 126803. (doi:10.1103/PhysRevLett.104.126803)

36. Ben Shalom, M. et al. 2010 Tuning Spin-Orbit Coupling and Superconductivity at the SrTiO3/LaAlO3 Interface: A Magnetotransport Study. *Phys. Rev. Lett.* **104**, 126802. (doi:10.1103/PhysRevLett.104.126802)

37. Caviglia, A. D. et al. 2008 Electric field control of the LaAlO3/SrTiO3 interface ground state. *Nature* **456**, 624. (doi:10.1038/nature07576)

38. Bell, C. et al. 2009 Dominant mobility modulation by the electric field effect at the laAlO3/SrTiO3 interface. *Phys. Rev. Lett.* **103**, 226802. (doi:10.1103/PhysRevLett.103.226802)

39. Fête, a. et al. 2012 Rashba induced magnetoconductance oscillations in the LaAlO 3-SrTiO3 heterostructure. *Phys. Rev. B* **86**, 201105(R). (doi:10.1103/PhysRevB.86.201105)

40. Hemberger, J. et al. 1995 Electric-field-dependent dielectric constant and nonlinear susceptibility in SrTiO3. *Phys. Rev. B* **52**, 13159. (doi:10.1103/PhysRevB.52.13159)

41. Ziman, J. M. 2001 *Electrons and phonons: the theory of transport phenomena in solids*. Oxford University Press.

42. Ashcroft, N. W. & Mermin, N. D. 1976 *Solid State Physics*. Harcourt College Publishers.

43. Biscaras, J. et al. 2012 Two-dimensional superconducting phase in LaTiO 3/SrTiO 3 heterostructures induced by high-mobility carrier doping. *Phys. Rev. Lett.* **108**, 247004. (doi:10.1103/PhysRevLett.108.247004)

44. Guduru, V. K. et al. 2013 Optically excited multi-band conduction in LaAlO3/SrTiO3 heterostructures. *Appl. Phys. Lett.* **102**, 051604. (doi:10.1063/1.4790844)

45. Guduru, V. K. et al. 2013 Multi-band conduction behaviour at the interface of LaAlO3/SrTiO3 heterostructures. *J. Korean Phys. Soc.* **63**, 437. (doi:10.3938/jkps.63.437)

46. Jost, A. et al. 2015 Transport and thermoelectric properties of the LaAlO_3/SrTiO_3 interface. *Phys. Rev. B* **91**, 045304. (doi:10.1103/PhysRevB.91.045304)

47. Pentcheva, R. et al. 2010 Parallel electron-hole bilayer conductivity from electronic interface reconstruction. *Phys. Rev. Lett.* **104**, 166804. (doi:10.1103/PhysRevLett.104.166804)

48. Sánchez, J. C. R. et al. 2013 Spin-to-charge conversion using Rashba coupling at the interface between non-magnetic materials. *Nat. Commun.* **4**, 2944. (doi:10.1038/ncomms3944)

49. Goniakowski, J. & Noguera, C. 2004 Electronic States and Schottky Barrier Height at Metal / MgO (100) Interfaces. *Interface Sci.* **12**, 93.

50. H, L. 2010 *Solid Surfaces, Interfaces and Thin Films*. Springer Berlin Heidelberg.

51. Tersoff, J. et al. 1984 Schottky mrier Heights and the Continuum of Gap States. *Phys. Rev. Lett.* **52**, 465. (doi:10.1103/PhysRevLett.52.465)

52. Dong, Y. F. et al. 2006 Ab initio studies on Schottky barrier heights at metal gate/LaAlO[sub 3] (001) interfaces. *Appl. Phys. Lett.* **89**, 122115. (doi:10.1063/1.2357012)

53. Singh-Bhalla, G. et al. 2010 Built-in and induced polarization across LaAlO_3/SrTiO_3 heterojunctions. *Nat. Phys.* **7**, 80. (doi:10.1038/nphys1814)

54. Delugas, P. et al. 2011 Spontaneous 2-dimensional carrier confinement at the n-type SrTiO 3/LaAlO3 interface. *Phys. Rev. Lett.* **106**, 166807. (doi:10.1103/PhysRevLett.106.166807)

55. Huang, B. C. et al. 2012 Mapping band alignment across complex oxide heterointerfaces. *Phys. Rev. Lett.* **109**, 246807. (doi:10.1103/PhysRevLett.109.246807)

56. Pauli, S. a et al. 2011 Evolution of the interfacial structure of LaAlO3 on SrTiO3. *Phys. Rev. Lett.* **106**, 036101. (doi:10.1103/PhysRevLett.106.036101)

57. Cazorla, C. & Stengel, M. 2012 First-principles modeling of Pt/LaAlO3/SrTiO3 capacitors under an external bias potential. *Phys. Rev. B* **85**, 075426. (doi:10.1103/PhysRevB.85.075426)

58. Reyren, N. et al. 2012 Gate-controlled spin injection at LaAlO 3/SrTiO 3 interfaces. *Phys. Rev. Lett.* **108**, 186802. (doi:10.1103/PhysRevLett.108.186802)

59. Gelatt, C. D. & Ehrenreich, H. 1974 Charge transfer in alloys: AgAu. *Phys. Rev. B* **10**, 398. (doi:10.1103/PhysRevB.10.398)

60. Michaelson, H. B. 1977 The work function of the elements and its periodicity. *J. Appl. Phys.* **48**, 4729. (doi:10.1063/1.323539)

61. Atkins, P. W. 1994 *Physical Chemistry*. 2nd Editio. Oxford University Press.

62. Ashcroft, S. J. & Schwarzmann, E. 1972 Standard enthalpy of formation of crystalline gold(III) oxide. *J. Chem. Soc. Faraday Trans. 1* **68**, 1360. (doi:10.1039/F19726801360)

63. Korobov, M. . et al. 1986 Enthalpy of formation of platinum hexafluoride. *J. Chem. Thermodyn.* **18**, 235. (doi:doi:10.1016/0021-9614(86)90051-0)

64. Lesne, E. 2015 Non-Equilibrium Spin Accumulation Phenomenon at the LaAlO3/SrTiO3(001) Quasi-Two-Dimensional Electron System.

65. Fête, A. 2015 Magnetotransport experiments at the LaAlO3/SrTiO3 interface.

66. M. Ohring 1992 *The Material Science of Thin Films*. Academic Press.

6

Annexes

Annex 1 – Growth Modes

During ablation of the target, species will randomly arrive at the surface of the substrate. If the diffusion length of these species is smaller than the terrace width, they will collide and stick with each other, forming island that will act as nucleation centers. The islands will grow and eventually will merge with nearby islands forming one layer of deposited material. This process is identified by the shape of the respective RHEED oscillation, as described in Methods.

In reality, the growth is never as perfect as described in the literature. A second layer may start to form while the first one is not yet complete, leading to intra-layer diffusion. Moreover, the oscillations are also influenced by the beam incidence angle chosen. The maximum intensity of each oscillation is therefore variable and will depend on such factors. The thickness of the grown layers gathered by RHEED is indeed not one hundred per cent accurate although it gives us a good estimation of the number of unit cells present. X-ray diffraction or transmission electron microscopy may be used to achieve more reliable values.

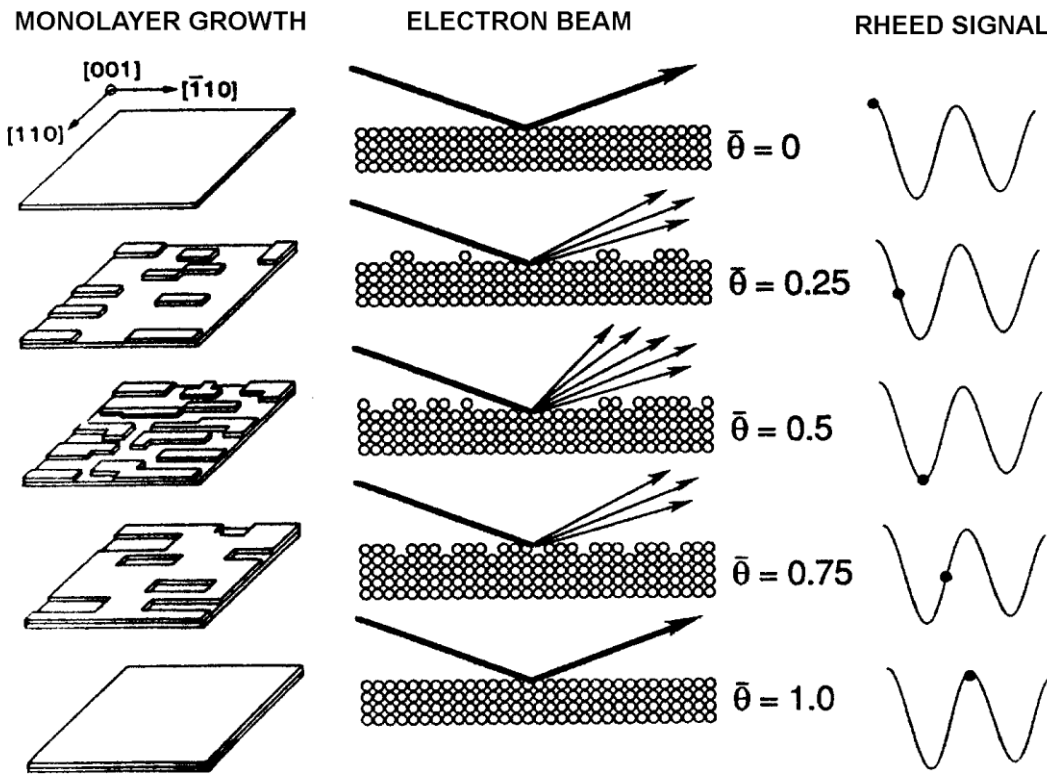

Annex Figure 1 – Formation of a single monolayer. The fractional layer coverage $\bar{\theta}$ is shown along with the corresponding RHEED oscillation signal [66].

Annex 2 – Antisymmetrization and Symmetrization Method

Antisymetrization (and symmetrization) is a mathematical process that converts any function into an antisymmetric (symmetric) function. On the upper left side of Annex Figure 2 we see that the raw Hall data gathered from the PPMS is not centered on zero. This should not be expected, since the absence of a magnetic field leads to no deviation of charged carriers, and therefore no voltage is measured (see right scheme of Figure 8). However, this effect highly depends on the perpendicularity of the contacts made. If contact I+ and I- do not make exactly 90° with contacts V+ and V-, a voltage will be present in the Hall measurement, even in the absence of an external field. Additionally since the data is gathered by sweeping the magnetic field from $0 \rightarrow 9T$, $9 \rightarrow 0T$, $0 \rightarrow -9T$ and $-9 \rightarrow 0T$, we

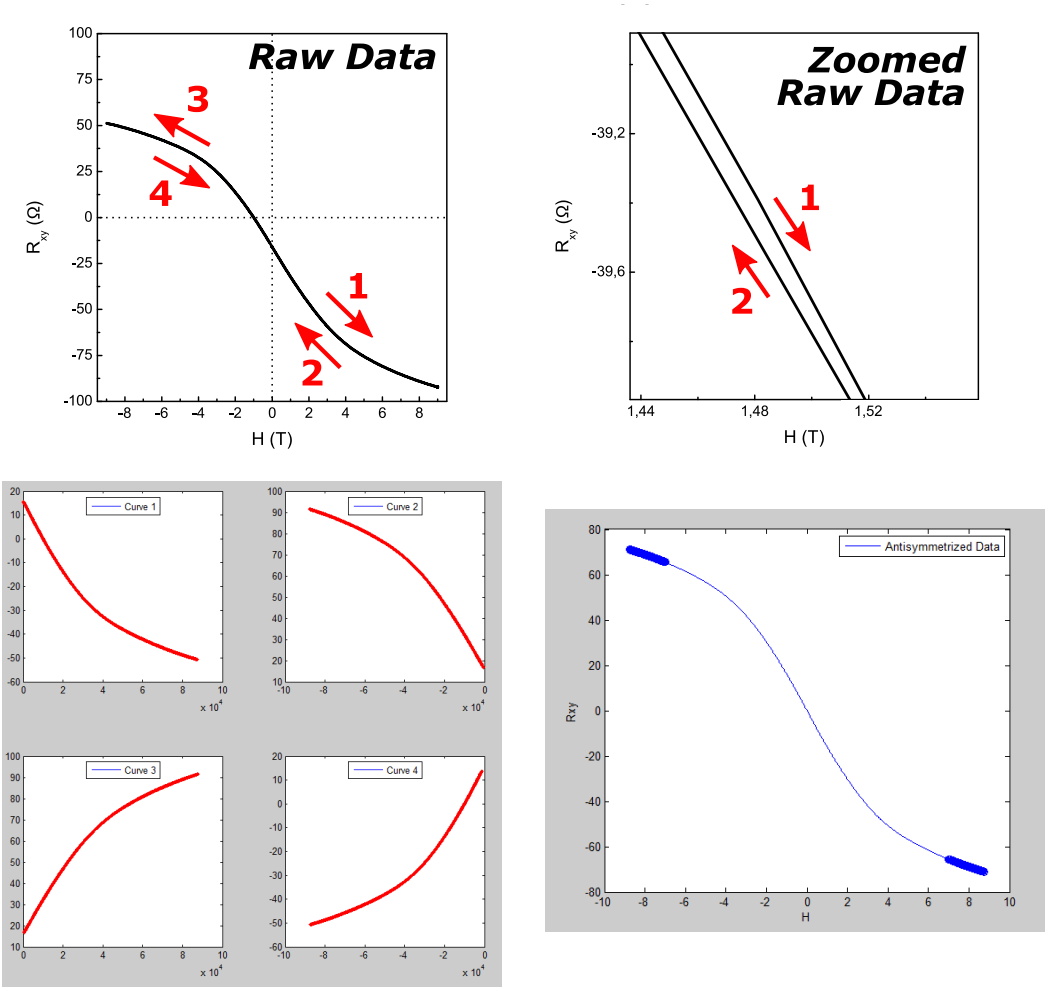

Annex Figure 2 – Antisymmetrizing data. Top left side the raw data got from the PPMS (and a zoomed plot that shows that the sweep is done in both direction). On the bottom the Matlab data treatment.

get four curves that will not perfectly coincide (a zoomed version of the raw data plot is shown on the upper right side of Annex Figure 2)

We developed an antisymmetrization (symmetrization) Matlab routine to correct these deviations. Four different curves are extracted, as shown on the bottom left side of Annex Figure 2. The positive field contribution is then averaged with the negative field contribution, resulting in two antisymmetrized curve (positive and negative field):

$$R_{xy}(H) = \frac{R_{xy}^{meas}(H) - R_{xy}^{meas}(-H)}{2} \qquad (19)$$

The final result is shown on the bottom right side, after applying eq. (19).

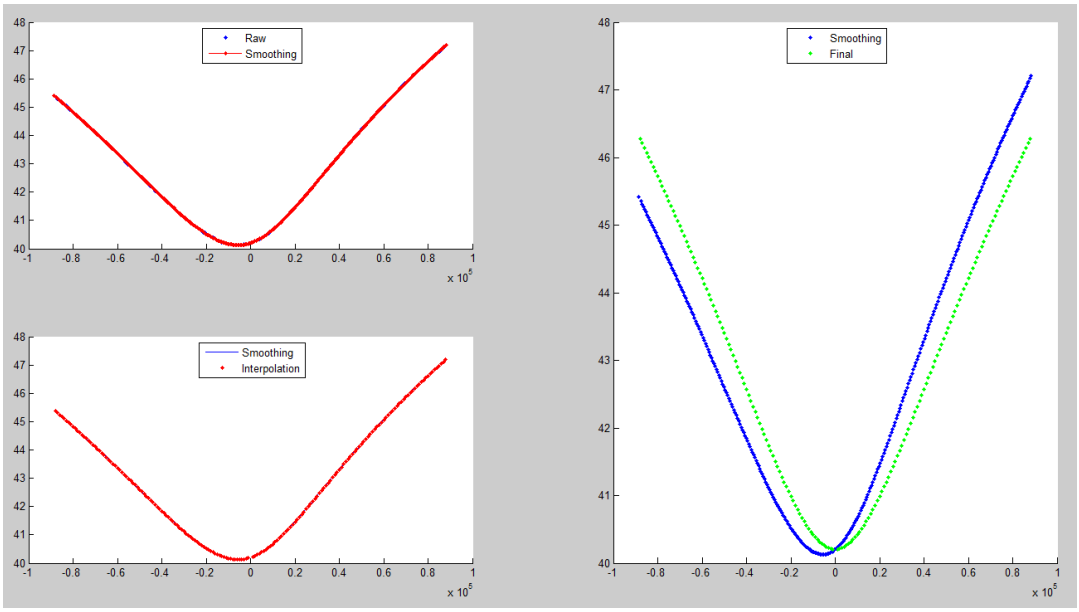

Annex Figure 3 – Symmetrized data. Top left side the smooth transverse resistance $\boldsymbol{R_{xx}^{meas}}$ (magnetoresistance). Bottom left side the interpolation made for a new array of magnetic field. On the right side the comparison between the smooth (blue) and symmetrized (green) data.

A similar procedure is used to symmetrize the data. In this case we take the raw transverse resistance R_{xx}^{meas} data for positive and negative fields and apply a 3-point smoothing with moving average filtering to attenuate noise from the PPMS measurement. The data is then linearly interpolated for a new array of fixed magnetic fields. The symmetrization is done using:

$$R_{xx}(H) = \frac{R_{xx}^{meas}(H) + R_{xx}^{meas}(-H)}{2} \tag{20}$$

The whole process is depicted in Annex Figure 3. On the right side the first smoothing (blue) is compared with the final symmetrized data (green).

Annex 3 – Experimental Setup

Annex Figure 4 – Experimental PLD and sputtering setup.

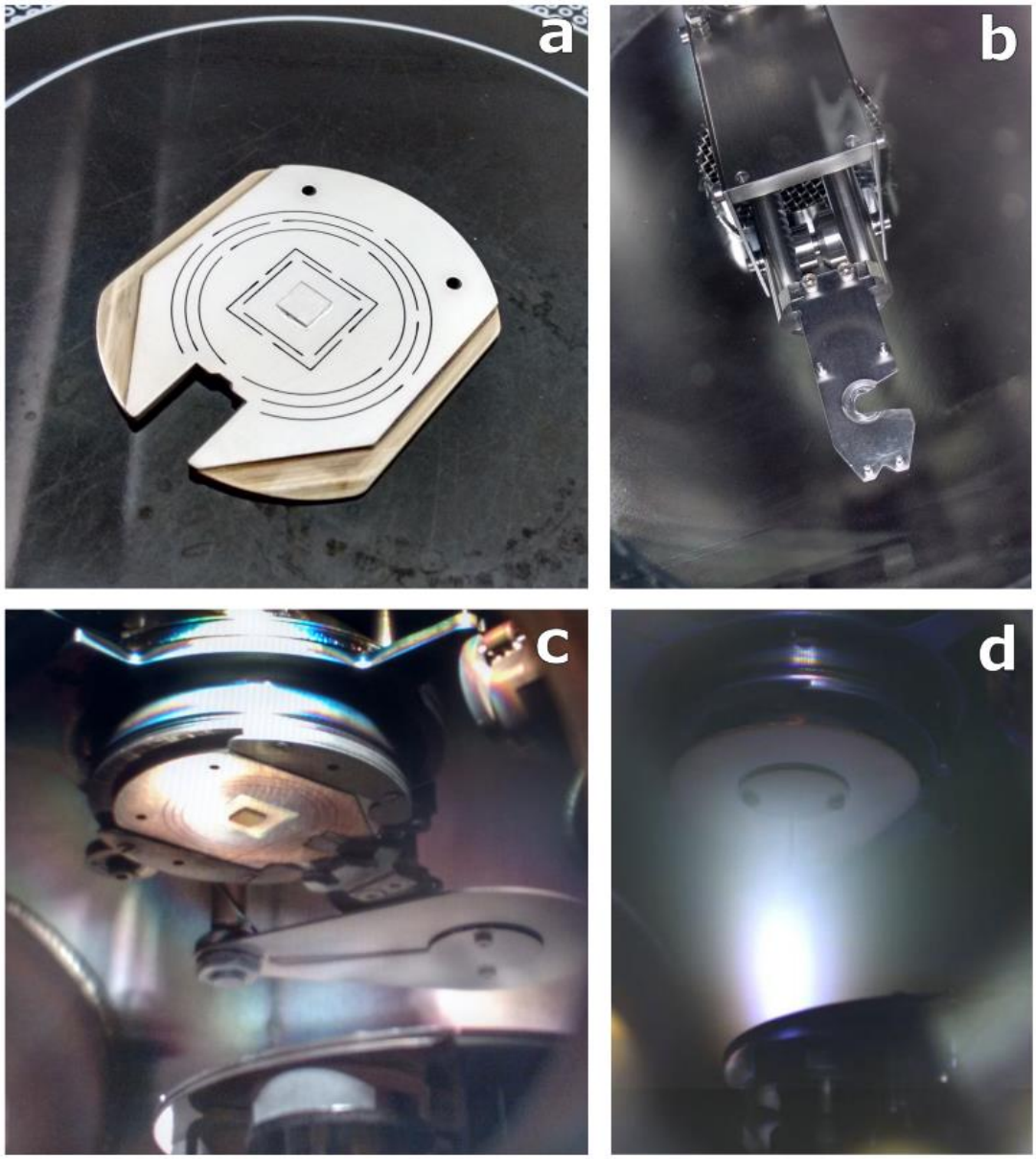

Annex Figure 5 – Growth process. a) A SrTiO3 substrate is glued with silver epoxy to a sample holder. The thin cuts deal with the holder expansion due to temperature. **b)** The arm inside the cluster (in vacuum) serves to move the sample holder between the loadlock, PLD chamber and sputtering chamber. The two pins on the back will attach to the holes of the sample holder. **c)** The sample holder is held upside down in the PLD chamber.In the middle we can also see the shutter and in the bottom the carousel with the targets. **d)** When the laser beam ablates the target, a plume is formed. This was the case of a pre-ablation process, where the shutter is placed in front of the sample.

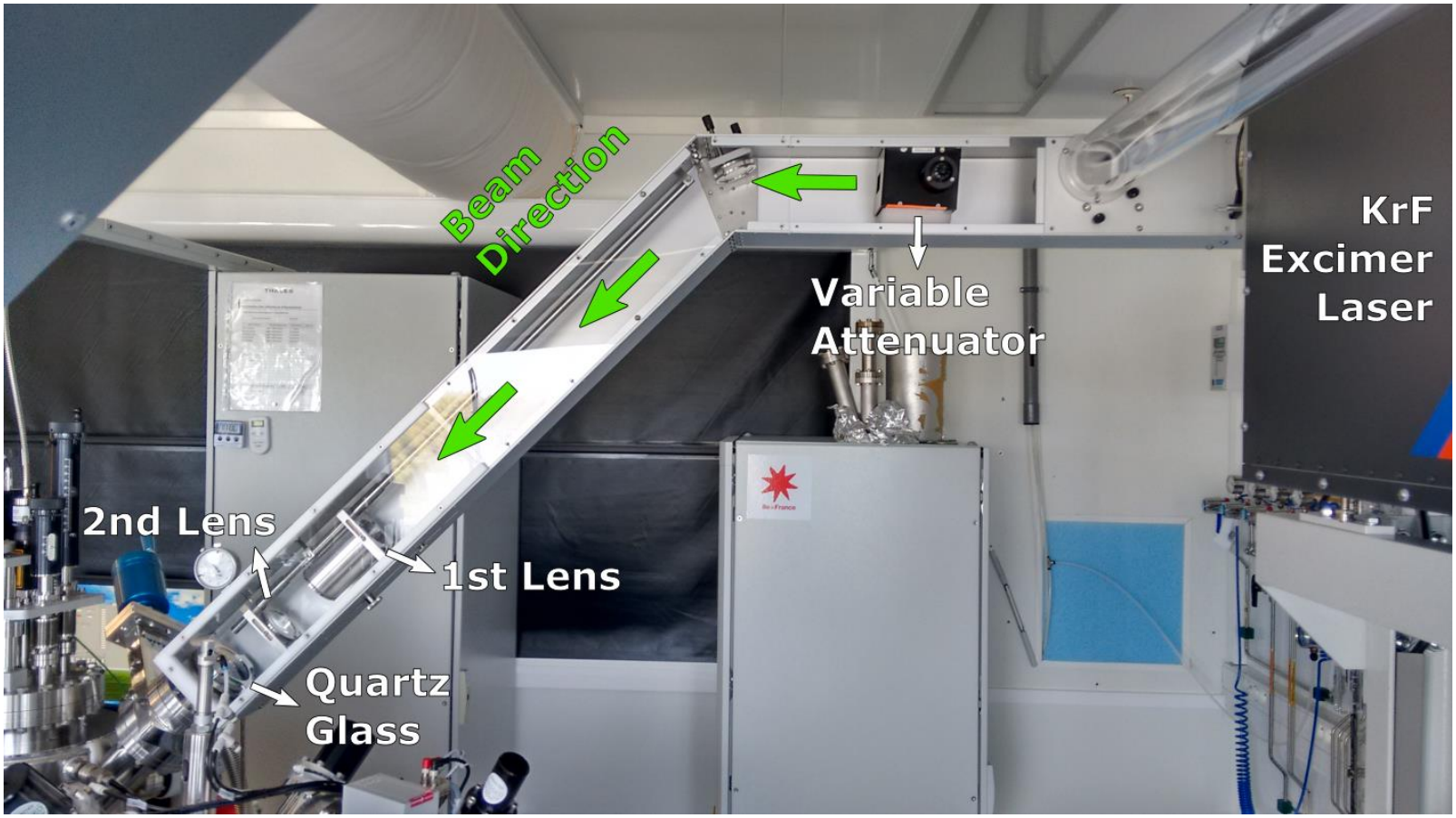

Annex Figure 6 – Optical path.

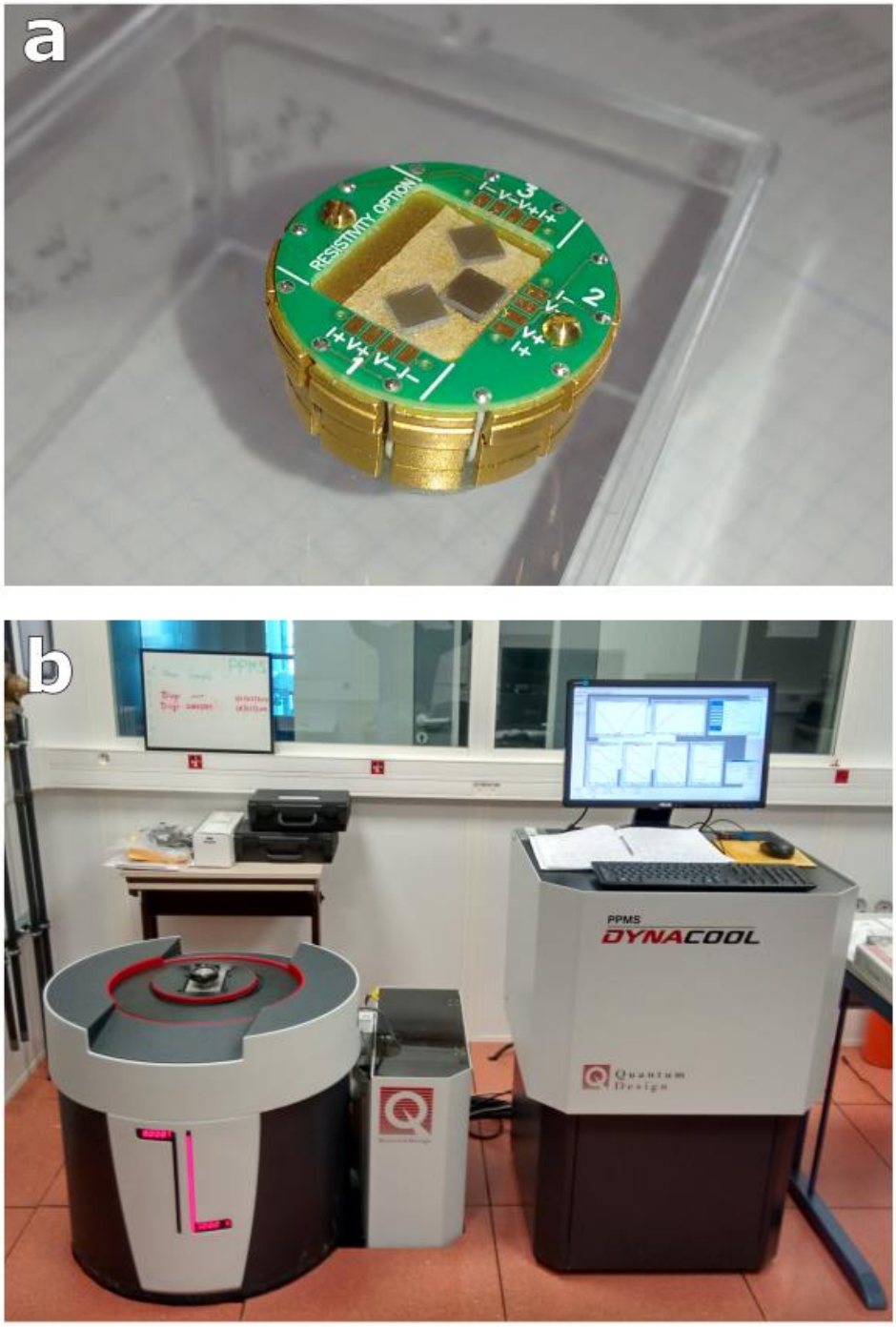

Annex Figure 7 – Quantum Design's PPMS Dynacool system. a) The puck used has three channels. Three samples can therefore be measured at the same time. **b)** The PPMS Dynacool allows programmed measurements at low temperatures (1.8K) and high magnetic fields (9T).

Magnetotransport properties of metal/$LaAlO_3$/$SrTiO_3$ heterostructures

Diogo Alexandre Castro Vaz (dac.vaz@campus.fct.unl.pt)

September 2015

Çim